

EVOLUTION OF MASSIVE PROTOSTARS VIA DISK ACCRETION

TAKASHI HOSOKAWA^{1,2,3}, HAROLD W. YORKE², KAZUYUKI OMUKAI^{1,3}*Draft version May 18, 2010*

ABSTRACT

Mass accretion onto (proto-)stars at high accretion rates $\dot{M}_* > 10^{-4} M_\odot \text{ yr}^{-1}$ is expected in massive star formation. We study the evolution of massive protostars at such high rates by numerically solving the stellar structure equations. In this paper we examine the evolution via disk accretion. We consider a limiting case of “cold” disk accretion, whereby most of the stellar photosphere can radiate freely with negligible backwarming from the accretion flow, and the accreting material settles onto the star with the same specific entropy as the photosphere. We compare our results to the calculated evolution via spherically symmetric accretion, the opposite limit, whereby the material accreting onto the star contains the entropy produced in the accretion shock front. We examine how different accretion geometries affect the evolution of massive protostars. For cold disk accretion at $10^{-3} M_\odot \text{ yr}^{-1}$ the radius of a protostar is initially small, $R_* \simeq$ a few R_\odot . After several solar masses have accreted, the protostar begins to bloat up and for $\dot{M}_* \simeq 10 M_\odot$ the stellar radius attains its maximum of $30 - 400 R_\odot$. The large radius $\sim 100 R_\odot$ is also a feature of spherically symmetric accretion at the same accreted mass and accretion rate. Hence, expansion to a large radius is a robust feature of accreting massive protostars. At later times the protostar eventually begins to contract and reaches the Zero-Age Main-Sequence (ZAMS) for $\dot{M}_* \simeq 30 M_\odot$, independent of the accretion geometry. For accretion rates exceeding several $10^{-3} M_\odot \text{ yr}^{-1}$ the protostar never contracts to the ZAMS. The very large radius of several $100s R_\odot$ results in a low effective temperature and low UV luminosity of the protostar. Such bloated protostars could well explain the existence of bright high-mass protostellar objects, which lack detectable H II regions.

Subject headings: accretion – stars: early-type – stars: evolution – stars: formation – stars: pre-main sequence

1. INTRODUCTION

Recent studies have revealed that the formation process of massive ($> 8 M_\odot$) stars differ in many respects from that of low-mass ($\sim 1 M_\odot$) stars (e.g., Zinnecker & Yorke 2007). Although signatures of mass accretion are widely observed toward forming massive stars, the estimated accretion rates usually exceed $10^{-4} M_\odot \text{ yr}^{-1}$, which are much higher than the typical value in low-mass star formation,

$$\dot{M}_* \sim \frac{c_s^3}{G} \simeq 5 \times 10^{-6} \left(\frac{T}{10 \text{ K}} \right) M_\odot \text{ yr}^{-1}, \quad (1)$$

where c_s and T is the sound speed and temperature in natal molecular cloud cores, and G is the gravity constant. In the past it has been argued that such high accretion rates are required for accretion flow to overcome the strong radiation pressure from forming massive stars (e.g., Larson & Starrfield 1971; Wolfire & Cassinelli 1987). However, these results were based on the assumption of spherically symmetric infall. Nevertheless, there are other good reasons to expect high accretion rates during the formation of massive stars: Massive stars have short Kelvin-Helmholtz time scales, once formed they con-

sume the available nuclear fuel quickly, and they will lose a significant part of their mass through strong stellar winds. Thus, massive stars evolve quickly, even while accreting. We can expect the time spent in the main accretion phase to be significantly less than the main sequence lifetime, presumably of the order of a few dynamical times of the star-forming molecular core. For a $30 M_\odot$ star this provides a lower limit to the average accretion rate $\simeq 10^{-4} M_\odot \text{ yr}^{-1}$. Accretion rates may vary strongly, however. Thus, phases of even higher accretion rates are likely.

The high accretion rates suggest that the nature of massive star formation differs from that of low-mass star formation. So far, various formation scenarios, such as monolithic collapse of massive dense cores (e.g., Yorke & Sonnhalter 2002; McKee & Tan 2002, 2003; Krumholz et al. 2007, 2009), and the competitive accretion with global infall of the cluster-forming clumps (e.g., Bonnell et al. 1998; Bonnell, Vine & Bate 2004; Wang et al. 2010), have been proposed. The proposed formation scenarios are being assessed with high-resolution observations of the massive cores and clumps (e.g., Motte et al. 2007; Marseille et al. 2008; Zhang et al. 2009; Bentemps et al. 2010).

The evolution of massive protostars at such high rates is a critical feature of massive star formation which determines the effect these stars have on their environment (e.g., Zinnecker & Yorke 2007). In our previous work (Hosokawa & Omukai 2008; 2009, hereafter Paper I), we examined the evolution by numerically solving the interior structure of a protostar with a dusty accretion enve-

¹ Department of Physics, Kyoto University, Kyoto 606-8502, Japan; hosokawa@tap.scphys.kyoto-u.ac.jp, omukai@tap.scphys.kyoto-u.ac.jp

² Jet Propulsion Laboratory, California Institute of Technology, Pasadena CA 91109; Takashi.Hosokawa@jpl.nasa.gov, Harold.Yorke@jpl.nasa.gov

³ Division of Theoretical Astronomy, National Astronomical Observatory, Mitaka, Tokyo 181-8588, Japan

lope under the assumption of spherical symmetry. Our calculations show that accreting massive protostars have certain characteristic features. At $\dot{M}_* = 10^{-3} M_\odot \text{ yr}^{-1}$, for example, the protostellar radius becomes very large, exceeding $100 R_\odot$ at maximum. The evolution before the arrival to the zero-age main sequence (ZAMS) lasts until $M_* \simeq 30 M_\odot$. At even higher accretion rates $\dot{M}_* > 3 \times 10^{-3} M_\odot \text{ yr}^{-1}$, the protostar very abruptly inflates and overtakes material in the inner part the accreting envelope, thus invalidating the assumption of steady mass accretion before reaching the ZAMS.

The very large stellar radius leads to a low effective temperature of the protostar, which in turn explains some observational properties of massive protostars in Orion KL nebula (Morino et al. 1998; Furuya & Shinaga 2009).

Observations suggest that mass accretion onto massive stars is not spherically symmetric, but rather proceeds through massive circumstellar disks (e.g., Cesaroni et al. 2007). Signatures of rotating infall are widely found toward forming massive stars, sometimes associated with massive outflows along the rotation axis (e.g., Patel et al. 2005; Beltrán et al. 2006a). Recent numerical simulations also suggest that the massive disk is a natural outcome of collapse of a massive dense core (Yorke & Sonnhalter 2002; Krumholz et al. 2007, 2009). Protostellar evolution via disk accretion has been studied for lower-mass protostars with low accretion rates $\dot{M}_* \leq 10^{-4} M_\odot \text{ yr}^{-1}$ (e.g., Palla & Stahler 1992; Beech & Mitalas 1994; Hartman et al. 1997). These authors considered the limiting case of “cold” disk accretion, whereby most of the stellar surface is able to radiate into free space and the accreting material brings only a small amount of entropy into the star. They showed that, with the low accretion rates, disk accretion slightly reduces the stellar radius compared to the spherically symmetric cases.

Maeder and coworkers studied the evolution of accreting massive protostars in the cold disk limit with mass accretion rates increasing with the stellar mass up to $10^{-4} M_\odot \text{ yr}^{-1}$ (e.g., Norberg & Maeder 2000; Behrend & Maeder 2001). Recently, Yorke & Bodenheimer (2008, hereafter YB08) calculated the evolution in the same limit with much higher accretion rates 10^{-3} and $10^{-2} M_\odot \text{ yr}^{-1}$. Their calculated evolution differs from the spherical accretion case in an early phase of $M_* \lesssim 8 M_\odot$. The stellar radius is several $10s R_\odot$ with spherical accretion, whereas it is a few R_\odot with disk accretion. However, YB08 find that the stellar radius rapidly increases soon afterwards and exceeds $100 R_\odot$ at $M_* \simeq 10 M_\odot$. The subsequent evolution at $M_* \gtrsim 10 M_\odot$ is quite similar for both spherical accretion and disk accretion.

In this paper, we examine how the different accretion geometries affect the evolution of massive protostars at high accretion rates. We explain why the two extreme cases lead to the same characteristic features of massive protostars, such as the large radius, in spite of the different evolution in the early phases. To this end, we calculate the protostellar evolution in the cold disk accretion limit with the numerical code used in Paper I. This allows us to extract how the protostellar evolution depends on the different accretion geometry independent

of the effects of different stellar evolution codes. For completeness, we also compare the calculated evolution with previous results by YB08.

Finally, we stress that this study is very relevant to star formation in the early universe, where high accretion rates are also expected. Protostellar evolution with high accretion rates has been studied with zero or very low metallicities under the assumption of spherically symmetric accretion (e.g., Stahler, Palla & Salpeter 1986; Omukai & Palla 2001, 2003; Hosokawa & Omukai 2009b). Recent numerical simulations show that circumstellar accretion disks are also expected during star formation in the early universe (Yoshida, Omukai & Hernquist 2008; Stacy, Grief & Bromm 2010). Tan & McKee (2004) examined the evolution of primordial protostars via disk accretion using simple analytic models. Here, we calculate the detailed evolution of a primordial protostar in the cold disk accretion limit.

The organization of this paper is as follows. The numerical method and the cases considered are briefly described in Section 2. In Section 3, we focus on the protostellar evolution at the accretion rate $\dot{M}_* = 10^{-3} M_\odot \text{ yr}^{-1}$, which allows a direct comparison to the results of YB08. First, we briefly review the evolution via spherical accretion studied in Paper I (Section 3.1), and then consider the evolution via cold disk accretion (Section 3.2). Evolution of a primordial protostar is investigated in Section 3.3 and subsequently contrasted to the present-day cases. Variation of the protostellar evolution with different accretion rates is studied in Section 4. Finally, Section 5 is devoted to our summary and conclusions.

2. NUMERICAL MODELING

2.1. Modeling Mass Accretion via Disks

We examine protostellar evolution by numerically solving the stellar structure equations. Case (a) in Figure 1 presents the schematic picture of the spherical accretion studied in Paper I, where we assumed spherical symmetry for an accretion envelope as well as the protostar. The numerical method we adopted is summarized as follows (e.g., Stahler, Shu & Taam 1980; also see Appendix A of Paper I). For a protostar, we solve the four stellar structure equations taking into account mass accretion. Free-fall flow is assumed for the optically thin part of the accretion envelope. If the accretion flow becomes opaque to the stellar radiation before hitting the stellar surface, we solve for the structure of this optically thick part of the flow together with the stellar structure equations of the protostar and the jump conditions at the accretion shock front. The accretion shock front is the outer boundary of the modeled protostar (shock boundary).

For the case of mass accretion via a circumstellar disk we consider the limiting case whereby the disk-star connecting layer is geometrically thin and most of the stellar surface is unlinked to the accretion flow. Figure 1 depicts this situation. In this case, the usual photospheric outer boundary condition can be applied for accreting protostars (e.g., Palla & Stahler 1992),

$$P_{\text{sf}} = \frac{2}{3} \frac{1}{\kappa_{\text{sf}}} \frac{GM_*}{R_*^2}, \quad (2)$$

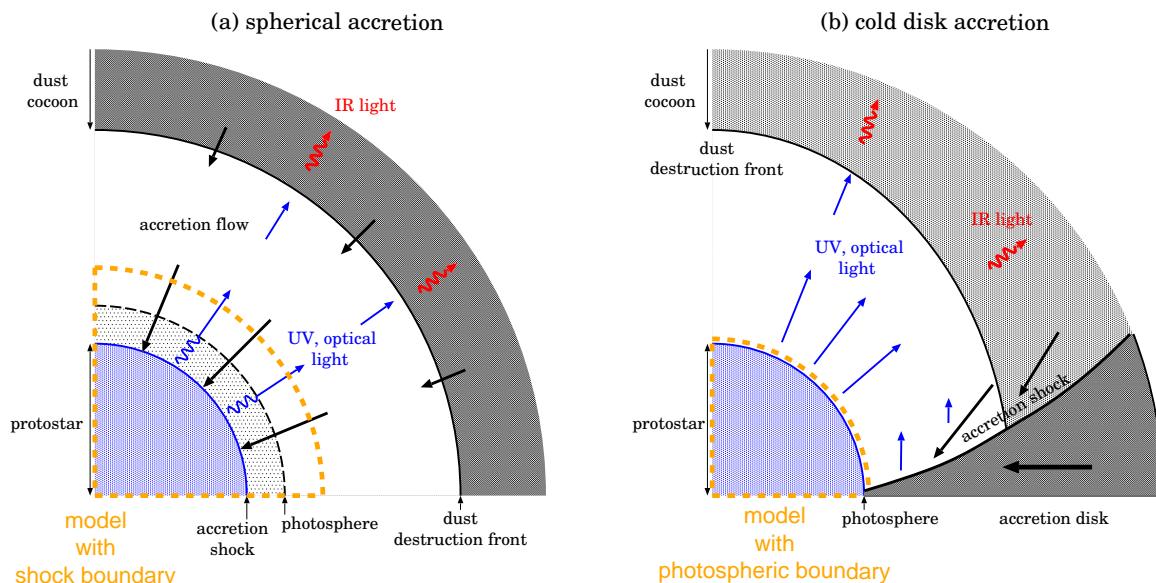


FIG. 1.— Schematic figures of a protostar with different accretion geometry: (a) spherically symmetric accretion, and (b) cold disk accretion. In the spherical case (a), the accretion flow directly hits the stellar surface forming an accretion shock front. If the flow is optically thick before reaching the surface, the photosphere locates outside the stellar surface. Dust grains in the accretion envelope evaporate in a dust destruction front far outside the photosphere. In the cold disk accretion case (b), gas predominantly accretes onto a circumstellar disk rather than the star. Accreting material settles onto the stellar surface through a geometrically thin layer (or possibly through geometrically thin accretion columns – not shown). Heat brought into the star in the accretion flow radiates freely into space until the temperature attains the photospheric value. Most of the stellar surface is unaffected by the accretion flow. The energy radiated away by the disk and/or accretion columns before the material settles onto the star (the so-called “accretion luminosity”) needs to be accounted for separately from the intrinsic stellar luminosity.

$$L_* = 4\pi R_*^2 \sigma T_{\text{sf}}^4, \quad (3)$$

where the suffix “sf” indicates the values at the stellar surface, and σ is Stefan-Boltzman constant. In this limiting case of disk accretion, accreting materials add to the star with the smallest amount of entropy, which is the value in the stellar atmosphere unattached to the accretion flow. Hence, the treatment with equations (2) and (3) supposes the limit of “cold” disk accretion. Note that this cold disk accretion is just a limiting case. Gas accreting onto the star through the disk is likely to have somewhat higher entropy especially at high accretion rates (Hartmann et al. 1997). The spherical accretion is the opposite limit where accreting materials carry the highest amount entropy into the star. Thus, we consider two extreme limiting cases with the spherical accretion and cold disk accretion. In order to solve the protostellar structure with cold disk accretion, we modified the numerical code used in Paper I to deal with the photospheric boundary condition. We do not solve the detailed structure of the flow connecting the star and disk.

Different geometries of the accretion flow will lead to different structures of the evolving protostar. For example, the average entropy in the stellar interior reflects the history of entropy brought into the star with accreting material, which in turn depend on the accretion geometry. For spherical accretion at high accretion rates the accretion shock front is embedded inside the stellar photosphere and most of the high entropy created at the accretion shock front is carried to the stellar surface. This entropy is efficiently taken into the stellar interior with high accretion rates (Paper I). As a result the protostar has a higher average entropy (compared to a non-accreting protostar), which leads to a very large radius – exceeding $100 R_\odot$ at maximum. With disk accretion,

however, entropy is mainly generated within the disk by viscous dissipation. Before the accreted material reaches the stellar surface, a large fraction of the generated entropy will be transported away by radiation. As a result, entropy brought into the star with the accreting material is significantly lower than in the spherical accretion case. The average entropy within the star s is related to the stellar radius as

$$R_* \propto M_*^{-1/3} \exp[\text{const.} \times s]. \quad (4)$$

This relation is derived by substituting the typical gas density and pressure within a star of mass M_* and radius R_* (e.g., Cox & Giuli 1968);

$$\rho \sim \frac{M_*}{R_*^3}, \quad P \sim G \frac{M_*^2}{R_*^4}, \quad (5)$$

to the definition of specific entropy of ideal monotonic gas,

$$s = \frac{3\mathcal{R}}{2\mu} \ln \left(\frac{P}{\rho^{5/3}} \right) + \text{const.}, \quad (6)$$

where \mathcal{R} is the gas constant and μ is the mean molecular weight. Equation (4) demonstrates that, for the same stellar mass, the stellar radius is larger with the higher average entropy in the stellar interior. Thus, we can naively expect that the stellar radius is reduced with disk accretion. Contrary to this expectation, however, calculations by YB08, adopting the cold disk accretion, show that the radius of a massive protostar exceeds $100 R_\odot$ at maximum as with the spherical accretion. The goal of this paper is to explain why the outcomes are so similar among the extreme cases of the spherical accretion and cold disk accretion.

Table 1. Input Parameters of the cases considered

Case	\dot{M}_* (M_\odot/yr) ^a	geometry	Z ^c	$M_{*,0}$ (M_\odot) ^d	$R_{*,0}$ (R_\odot) ^e	reference ^f
MD4x3-SDm0.5 ^g	4×10^{-3}	S \rightarrow D	0.02	0.3 (0.5)	32.7 (36.8)	Section 4
MD4x3-S	4×10^{-3}	S	0.02	0.3	32.7	Section 4, Paper I
MD3-D	10^{-3}	D	0.02	0.1	3.7	Section 3.2
MD3-D-b0.1	10^{-3}	D	0.02	0.1	3.5	Section 3.2.2
MD3-D-cv	10^{-3}	D	0.02	1.3	6.2	Section 3.2.2
MD3-S	10^{-3}	S	0.02	0.05	15.5	Section 3.1, Paper I
MD3-S-z0	10^{-3}	S	0.0	0.05	13.0	Section 3.3, Paper I
MD3-SDm1	10^{-3}	S \rightarrow D	0.02	0.05 (1.0)	15.5 (24.4)	Section 3.2.2
MD3-SDm0.1	10^{-3}	S \rightarrow D	0.02	0.05 (0.1)	15.5 (14.1)	Section 3.2.2
MD3-SDm0.1-z0	10^{-3}	S \rightarrow D	0.0	0.05 (0.1)	13.0 (14.1)	Section 3.3
MD4-S	10^{-4}	S	0.02	0.03	8.8	Section 4, Paper I
MD4-SDm0.1	10^{-4}	S \rightarrow D	0.02	0.03 (0.1)	8.8 (5.1)	Section 4
MD4-D-cv	10^{-4}	D	0.02	1.3	6.2	Appendix B.1
MD5-D-cv	10^{-5}	D	0.02	1.0	4.3	Appendix B.1
MD5-S-cv	10^{-5}	S	0.02	1.0	4.2	Appendix B.1, Paper I

a : mass accretion rate, *b* : geometry of the accretion flow (D: disk accretion, S: spherical accretion), *c* : metallicity, *d* : mass of initial core model, *e* : radius of initial core model, *f* : subsections where numerical results of each case are presented. *g* : the suffix SDmX means the geometry is switched from spherical accretion to disk accretion at $\dot{M}_* = X M_\odot$. For these cases, stellar mass and radius at the switching point are listed in the brackets in the columns of $M_{*,0}$ and $R_{*,0}$.

2.2. Cases considered

Table 1 summarizes the cases considered in this study and their input parameters. For simplicity the protostellar evolution is calculated with a constant given accretion rate for each case. The adopted accretion rates range from $10^{-5} M_\odot \text{ yr}^{-1}$ up to $4 \times 10^{-3} M_\odot \text{ yr}^{-1}$. Evolution for the accretion rate $\dot{M}_* = 10^{-3} M_\odot \text{ yr}^{-1}$ is studied in detail. In addition to evolution with cold disk accretion we present several cases with spherical accretion for comparison. Evolution via disk accretion at the rates $\dot{M}_* = 10^{-5} M_\odot \text{ yr}^{-1}$ and $10^{-4} M_\odot \text{ yr}^{-1}$ was also studied by Palla & Stahler (1992). We consider protostellar evolution with these low rates to compare our results with theirs (see Appendix B.1).

The initial model in each case is constructed following Stahler, Shu & Taam (1980) or Palla & Stahler (1991) with the adopted accretion rate and boundary conditions (also see Appendix A.2 and B.2 in Paper I). The initial stellar mass $M_{*,0}$ is taken as an arbitrary small value. The initial entropy profile in the stellar interior is assumed as a function of the mass coordinate M ,

$$s(M) = s_{c,0} + \beta \frac{k_B}{m_H} \frac{M}{M_{*,0}}, \quad (7)$$

where $s_{c,0}$ is specific entropy at the stellar center, k_B is Boltzmann constant, m_H is atomic mass unit, and β (> 0) is a free parameter. We adopt $\beta = 1$ as a fiducial value. Unlike the cases of spherical accretion, however, we will see that the protostellar evolution with the photospheric boundary changes with different initial models even at the same accretion rate (see Section 3.2.2 below). We show this by presenting the evolution with different initial models with $\beta = 0.1$ (shallower entropy profile, case MD3-D-b0.1), and $\beta = 0$ (homogeneous entropy profile, cases with the suffix “cv”).

The geometry of the accretion flow will vary as a function of the stellar mass and radius. Initially, the collapse of a gravitationally unstable molecular core is mostly spherically symmetric. A hydrostatic object is formed when the central regions of the molecular core become optically thick. A circumstellar disk is later formed

as material with increasingly higher angular momentum falls toward the newly formed protostar. For these cases we start the protostellar evolution calculation assuming spherical accretion and later switch to cold disk accretion (cases with the suffix “SD”). We also present the evolution of primordial protostars via disk accretion (case MD3-SDm0.1-z0).

3. EVOLUTION OF MASSIVE PROTOSTARS WITH $\dot{M}_* = 10^{-3} M_\odot \text{ yr}^{-1}$

3.1. Spherically Symmetric Accretion

Here, we briefly review the evolution with spherically symmetric accretion studied in Paper I. The upper panel of Figure 2 shows the evolution of the stellar radius and interior structure at the accretion rate $\dot{M}_* = 10^{-3} M_\odot \text{ yr}^{-1}$ (case MD3-S). We define the following four evolutionary phases from the behavior of the stellar radius: (I) gradual expansion ($M_* \lesssim 6 M_\odot$), (II) swelling ($6 M_\odot \lesssim M_* \lesssim 10 M_\odot$), (III) contraction ($10 M_\odot \lesssim M_* \lesssim 30 M_\odot$), (IV) gradual expansion ($M_* \gtrsim 30 M_\odot$). A key quantity to understand the variety of the evolution is the ratio between the accretion timescale,

$$t_{\text{acc}} \equiv \frac{M_*}{\dot{M}_*}, \quad (8)$$

and the Kelvin-Helmholtz (KH) timescale,

$$t_{\text{KH}} \equiv \frac{GM_*^2}{R_* L_*}. \quad (9)$$

The former is the evolutionary timescale, and the latter is the timescale over which a star loses energy by radiation. The lower panel of Figure 2 displays the evolution of these timescales. We see that t_{KH} significantly decreases during phase (II). As a result, the balance of these timescales changes from $t_{\text{acc}} \ll t_{\text{KH}}$ in phase (I) to $t_{\text{acc}} > t_{\text{KH}}$ in phase (III) and (IV). The decrease of t_{KH} is caused by a rapid increase of the stellar luminosity L_* , which in turn is a result of the decrease in opacity. In most of the stellar interior the opacity’s dependence on density and temperature is approximated by Kramers’ law $\kappa \propto \rho T^{-3.5}$. Thus, as the stellar mass increases,

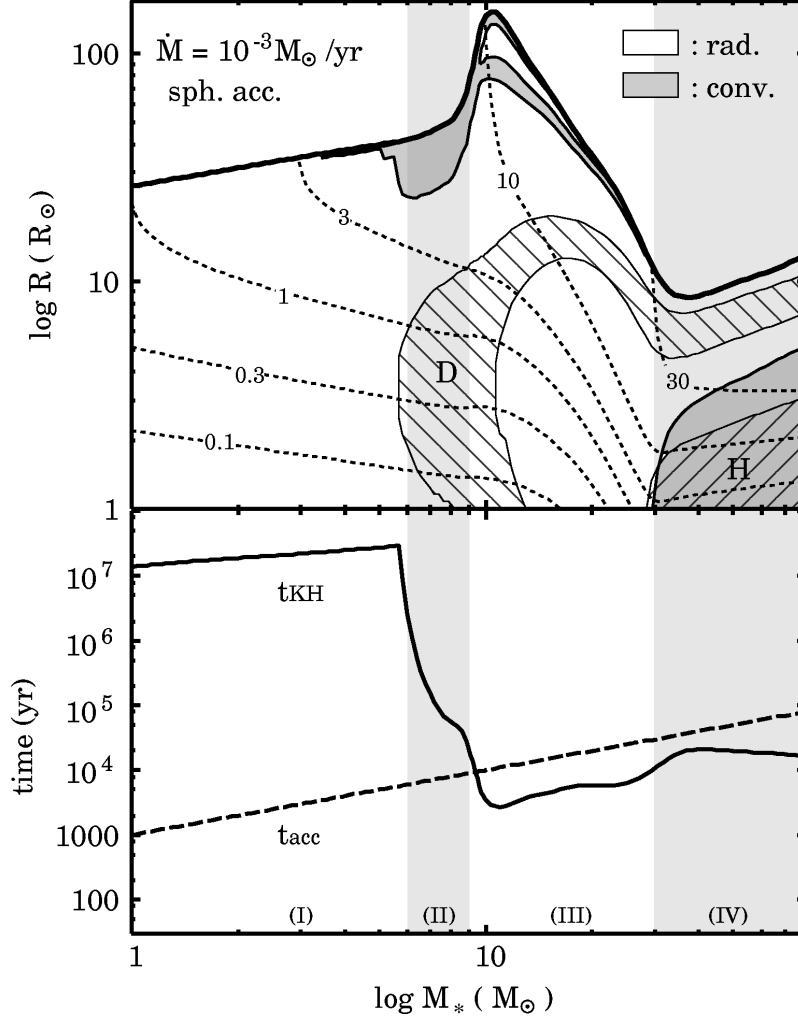


FIG. 2.— Evolution of a protostar via spherical accretion at a rate $\dot{M}_* = 10^{-3} M_\odot \text{ yr}^{-1}$ (case MD3-S, taken from Paper I). *Upper panel:* Evolution of the interior structure of the protostar. The gray-shaded areas denote convective layers. The hatched areas indicate layers with active nuclear burning, where the energy production rate exceeds 10% of the steady rate $0.1L_{D,\text{st}}/M_*$ for deuterium burning and $0.1L_*/M_*$ for hydrogen burning. The thin dotted curves show the locations of mass coordinates $M = 0.1, 0.3, 1, 3, 10$, and $30 M_\odot$. *Lower panel:* Evolution of the accretion timescale t_{acc} (dashed line), and Kelvin-Helmholtz timescale t_{KH} (solid line). In each panel the shaded background denotes the four evolutionary phases; (I) adiabatic accretion, (II) swelling, (III) Kelvin-Helmholtz contraction, and (IV) main sequence accretion phases.

the temperature in the interior rises and the opacity decreases.

Figure 3 shows snapshots of radial profiles of entropy and luminosity in the early phases (I) and (II). At the assumed high accretion rate the entropy is initially efficiently brought into the stellar interior with minimal radiative loss because of the high opacity during phase (I). The instantaneous entropy profile simply traces the post-shock values from earlier times (adiabatic accretion). The average entropy within the star increases with accreted mass, which according to equation (4) means that the stellar radius should also grow. This is indeed the case in phases (I) and (II). As the average density decreases and the temperature increases, the opacity decreases; radiative heat transport becomes more efficient with increasing stellar mass.

For $M_* \gtrsim 6 M_\odot$ (phase II) radiative heat transport is efficient enough to modify the entropy distribution

within the star. The deep interior (where $\partial L/\partial M > 0$) loses entropy, whereas the outer surface regions (where $\partial L/\partial M < 0$) gain a significant amount of entropy. This gain in entropy results in the “bloating up” of the star up to $\gtrsim 100 R_\odot$ at maximum. Figure 3 shows that the boundary between the heat-losing interior and heat-gaining outer layer, namely where $\partial L/\partial M = 0$, moves toward the stellar surface with increasing stellar mass. Stahler, Palla & Salpeter (1986) called this characteristic behavior of luminosity profiles a “luminosity wave”. The stellar surface luminosity L_* rapidly increases when the luminosity wave approaches the stellar surface. After the luminosity wave passes through the surface, the star can efficiently lose energy by radiation. The star contracts to maintain virial equilibrium (Kelvin-Helmholtz or KH contraction; phase III). The interior temperature rises during the contraction. Active hydrogen burning begins when the central temperature exceeds 10^7 K. After that,

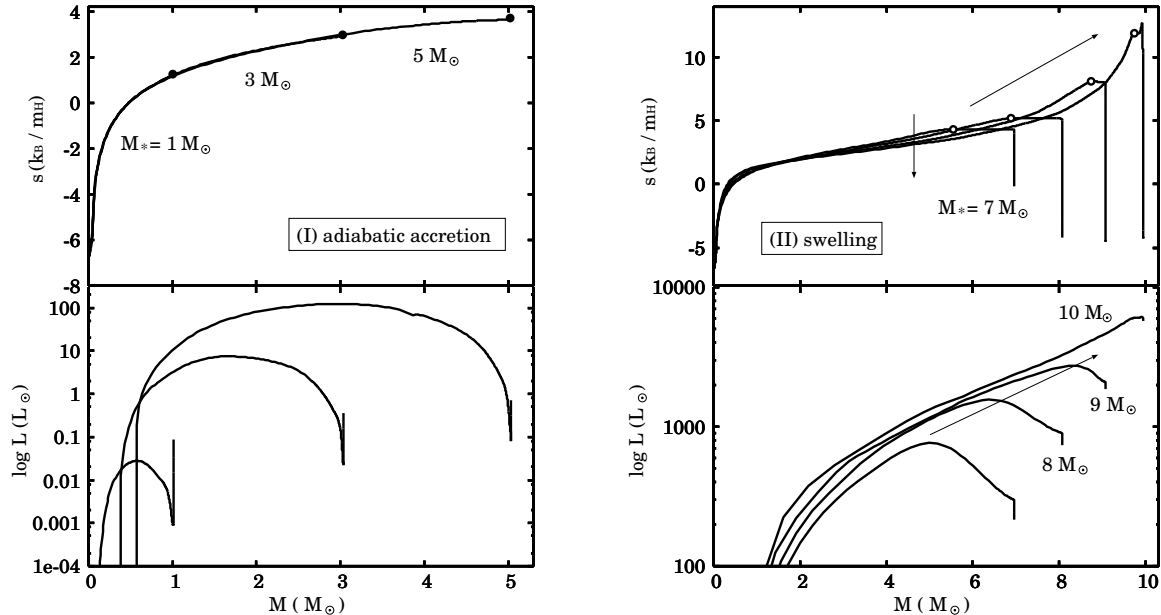


FIG. 3.— Radial profiles of the specific entropy and luminosity assuming spherical accretion at a rate $\dot{M}_* = 10^{-3} M_\odot \text{ yr}^{-1}$ (case MD3-S, taken from Paper I). Each profile is shown as a function of the mass coordinate M . The two panels display representative profiles during the first two evolutionary phases: (I) adiabatic accretion (left), and (II) swelling phase (right). The filled circles on the entropy profiles in the left panel indicate the post-shock values. The open circles in the right panel show the values for the bottom edges of the convective layers.

the stellar radius increases following the mass-radius relation of main sequence stars (phase IV).

3.2. Case with Cold Disk Accretion

3.2.1. Fiducial Model

We now consider stellar evolution with cold disk accretion at the same rate $\dot{M}_* = 10^{-3} M_\odot \text{ yr}^{-1}$ (case MD3-D). First, we discuss the fiducial case with the $0.1 M_\odot$ initial model adopting $\beta = 1$ in equation (7). The top panel of Figure 4 shows the evolution of the stellar radius and interior structure. We see that the evolution differs from the spherical accretion case for $M_* \lesssim 10 M_\odot$, as previously demonstrated by YB08 (also see Appendix B.2 for comparison to YB08). For $M_* \lesssim 5 M_\odot$ the stellar radius is much smaller than for spherical accretion. An outer convective zone appears in this phase. The protostar then abruptly inflates during the period $5 M_\odot \lesssim M_* \lesssim 9 M_\odot$. The maximum radius is $\simeq 90 R_\odot$ for $M_* \simeq 10 M_\odot$, which is comparable to the results of the spherical accretion case. The stellar radius decreases for $M_* \gtrsim 10 M_\odot$, and then finally follows the mass-radius relationship for main sequence stars when $M_* \gtrsim 30 M_\odot$. The evolution for $M_* \gtrsim 10 M_\odot$ is quite similar to what we discussed above for spherical accretion.

We define the following four phases based on the evolutionary features: (I) convection ($M_* \lesssim 5 M_\odot$), (II) swelling ($5 M_\odot \lesssim M_* \lesssim 9 M_\odot$), (III) KH contraction ($9 M_\odot \lesssim M_* \lesssim 30 M_\odot$), and (IV) main sequence accretion phase ($M_* \gtrsim 30 M_\odot$). The top panel of Figure 5 shows the evolution of the accretion timescale and KH timescale. We note that t_{KH} significantly decreases at $M_* \simeq 6 M_\odot$, when the protostar rapidly inflates. The timescale balance sharply changes from $t_{\text{acc}} \ll t_{\text{KH}}$ to $t_{\text{acc}} > t_{\text{KH}}$ here. As with spherical accretion, we attribute the sequence of the evolutionary phases from (I)

to (III) to the inversion of the timescale balance. The lower panel of Figure 5 shows that this change is due to the rapid increase of stellar luminosity L_* caused by the decrease of opacity in the stellar interior with increasing mass. The detailed evolution in each phase is explained below.

Convection Phase— The top panels of Figures 2 and 4 show that the evolution at $M_* \lesssim 5 M_\odot$ is quite different between the spherical accretion case and disk accretion case. In the disk accretion case the protostellar radius is about one tenth of the value obtained for spherical accretion. This is explained by equation (4) and the fact that the entropy content within the star is much lower with disk accretion, a natural consequence of the different accretion geometry. With spherically symmetric accretion gas settles onto the star with high entropy generated in the accretion shock front. For cold disk accretion, on the other hand, the entropy of the accreting gas is reduced to the value in the stellar atmosphere by the gas' ability to radiate into free space. Mass accretion hardly affects the average entropy in the stellar interior for the case of cold disk accretion. Equation (4) shows that the stellar radius decreases according to $R_* \propto M_*^{-1/3}$ in this case. We see this decrease for $M_* \lesssim 0.5 M_\odot$ in Figure 4.

Figure 4 shows that deuterium burning (D-burning) begins when $M_* \simeq 0.4 M_\odot$. This is in stark contrast to the spherical accretion case, where it begins much later ($M_* \simeq 6 M_\odot$), as shown in Figure 7. This difference reflects the different evolution of the maximum temperature within the protostar T_{max} (middle panel of Fig. 4). The early rise of T_{max} with disk accretion is explained by the relation,

$$T = \frac{\mu}{\mathcal{R}} \frac{P}{\rho} \propto \frac{M_*}{R_*}, \quad (10)$$

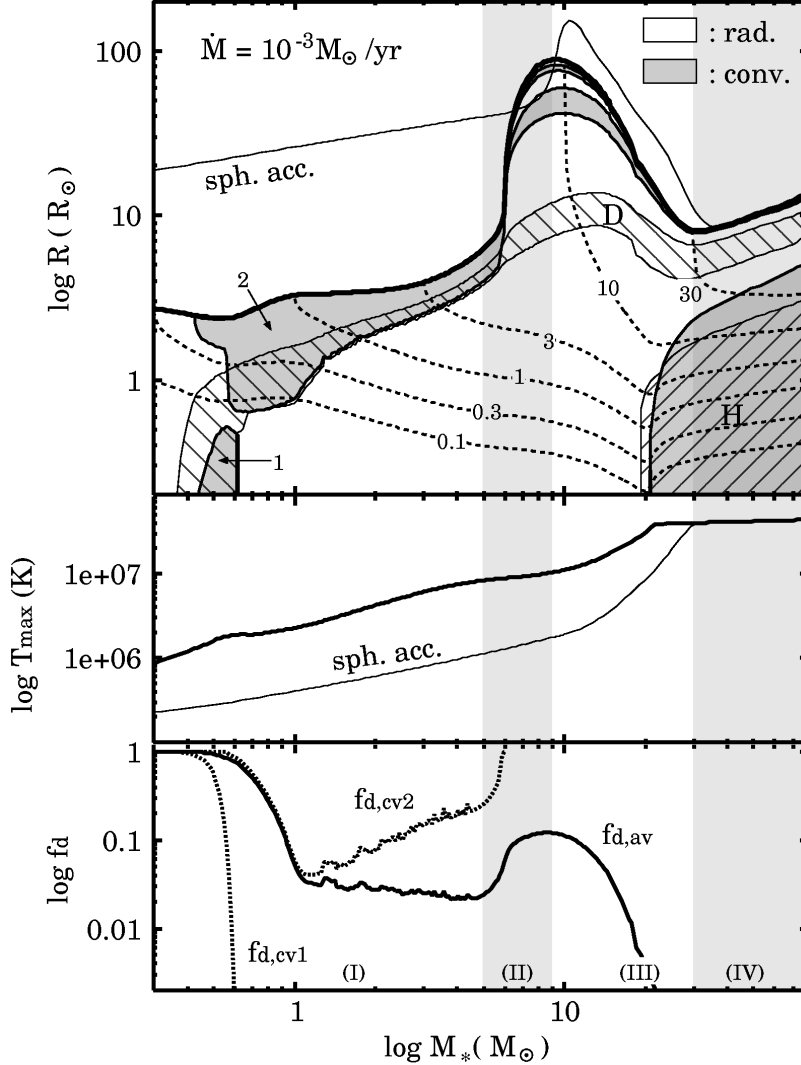


FIG. 4.— Evolution of a protostar via disk accretion at the rate $\dot{M}_* = 10^{-3} M_{\odot} \text{ yr}^{-1}$ (case MD3-D). *Top panel* : Evolution of the interior structure of a protostar. Illustration of the figure is the same as in the upper panel of Fig. 2. The thin solid line represents the evolution of the radius via spherical accretion at the same rate (case MD3-S, taken from Paper I). *Middle panel* : Evolution of the maximum temperature within the star T_{max} . Values for spherical accretion at the same rate are plotted with a thin solid line. In this figure the shaded background shows the four evolutionary phases; (I) convection, (II) swelling, (III) Kelvin-Helmholtz contraction, and (IV) main sequence accretion phases. *Bottom panel* : Evolution of the deuterium concentrations of convective layers $f_{d,cv1/2}$ (dotted lines), and mass-averaged deuterium concentration, $f_{d,av}$ (solid line).

where T is the typical temperature within the star \mathcal{R} is the gas constant, and μ is the mean molecular weight. Equations (5) were used again to derive the dependence on M_*/R_* . Equation (10) means that, at the same stellar mass, the interior temperature is higher for the smaller stellar radius. Since the stellar radius R_* is smaller for the disk accretion, the central temperature is higher for the same stellar mass. Thus, D-burning begins much earlier in the disk accretion case.

Figure 4 shows that convective zones emerge soon after deuterium burning begins. First, a convective zone appears near the center for $M_* \simeq 0.5 M_{\odot}$. However, this zone disappears soon, when available deuterium is exhausted. The D-burning layer moves to the outer part of the star, where fresh deuterium still remains. Another convective zone forms there, connecting the D-burning layer to the stellar surface, where newly accreted deu-

terium can be mixed down to the D-burning layer. When $M_* \gtrsim 1 M_{\odot}$ the total energy production rate by D-burning becomes nearly equal to the steady-state rate (bottom panel of Fig. 5),

$$L_{D,st} \equiv \dot{M}_* \delta_D = 1500 L_{\odot} \left(\frac{\dot{M}_*}{10^{-3} M_{\odot}/\text{yr}} \right) \left(\frac{[D/H]}{2.5 \times 10^{-5}} \right), \quad (11)$$

where δ_D is the energy available from the deuterium burning per unit gas mass.

For $M_* \gtrsim 1 M_{\odot}$, the radiative core extends outward and the outer convective layer with its D-burning shell becomes geometrically thinner. This evolution is a result of the decrease of opacity in the stellar interior; radiative heat transport becomes more efficient with the lower opacity. At the end of phase (I) convection ceases where

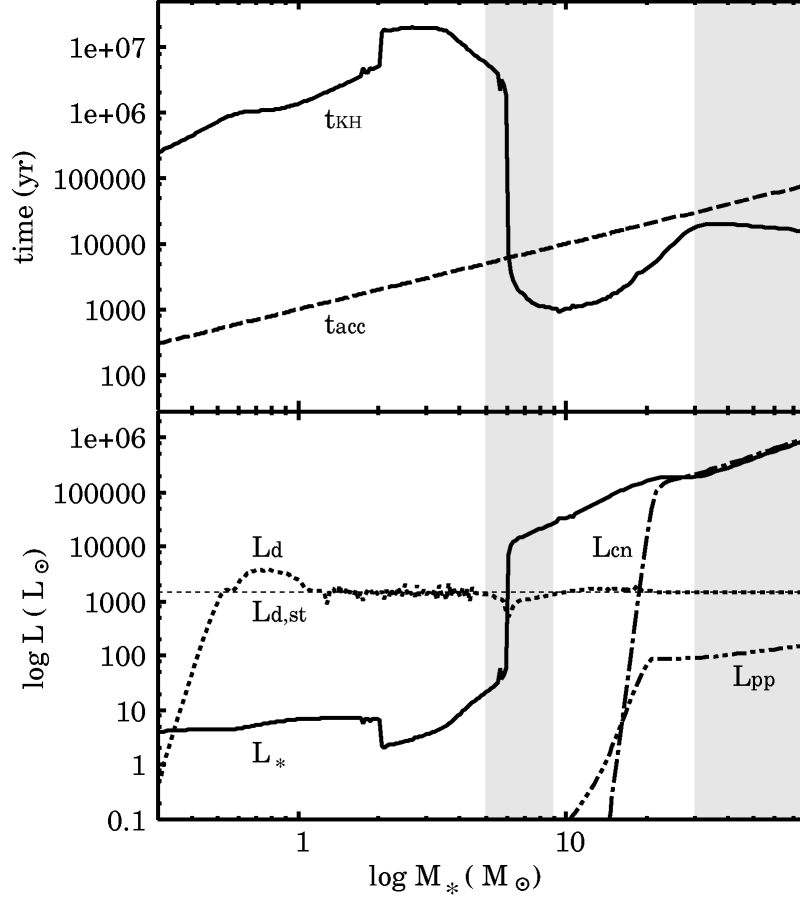


FIG. 5.— *Upper panel:* Evolution of the accretion timescale t_{acc} (dashed line) and Kelvin-Helmholtz timescale t_{KH} (solid line). *Lower panel:* Evolution of various contributions to the luminosity of the protostar. The thick solid line depicts the luminosity at the stellar surface L_* . The total energy production rate by each type of nuclear reaction is shown for 1) deuterium burning (L_d , coarse dotted), 2) pp-chain (L_{pp} , dot-dot-dashed), and 3) CNO-cycle (L_{CN} , dot-dashed line). The thin dashed horizontal line indicates the steady deuterium burning rate $L_{d,\text{st}}$. In each panel the shaded background denotes the four evolutionary phases as in Fig. 4.

the radiative heat transport is efficient enough to carry away the heat generated by deuterium burning. Fresh deuterium is no longer supplied to the D-burning layer which has now become radiative.

Figure 4 shows that the stellar radius gradually increases after the ignition of deuterium burning. This is because deuterium burning enhances the average entropy in the stellar interior. The surface convective layer absorbs the entropy generated by deuterium burning. Figure 6-(I) clearly shows that the entropy in the surface convective layer rises with increasing stellar mass. The effect of deuterium burning is also seen in Figure 7, which depicts the evolution of the stellar radius when deuterium burning is artificially turned off at some point (dashed lines). We see that, if deuterium burning is turned off at $M_* = 3 M_\odot$, the stellar radius ceases to increase.

Figure 7 also presents the evolution via spherical accretion without deuterium burning (dashed line). We see that, unlike the case of disk accretion explained above, deuterium burning hardly affects the evolution. A key quantity to interpret this difference is the opacity when deuterium burning begins. With spherical accretion, deuterium burning begins late, when $M_* \simeq 6 M_\odot$ and the opacity within the star has already decreased sufficiently. The radiative heat transport is so efficient that the heat generated by deuterium burning is carried away

before the convection arises. With disk accretion, on the other hand, the opacity is still high at the ignition of deuterium burning when $M_* \simeq 0.3 M_\odot$. Deuterium burning initiates the convection due to the inefficient radiative heat transport. In this case deuterium burning affects the stellar evolution until opacity becomes low enough owing to increasing the stellar mass.

Swelling Phase— The stellar radius rapidly increases in this phase. However, this is not a homologous expansion of the star. Only a small percent of the mass near the surface significantly bloats up. For $M_* \simeq 10 M_\odot$, for example, 10% of the total stellar mass fills 90% of the radius and 99.9% of the volume. Figure 4 also shows that the stellar interior structure changes during the swelling. The surface convective zone leaves the D-burning layer and moves outward for $M_* \simeq 6 M_\odot$. The radiative core covers most of the stellar interior.

What is the mechanism of the significant swelling? We contend that deuterium burning cannot be the primary cause, as demonstrated in the top panel of Figure 7. We see that, even if we completely (artificially) turn off deuterium burning, the protostar subsequently inflates in all examined cases. Deuterium burning enhances the swelling, however; the earlier deuterium burning is turned off, the later the swelling occurs with a smaller

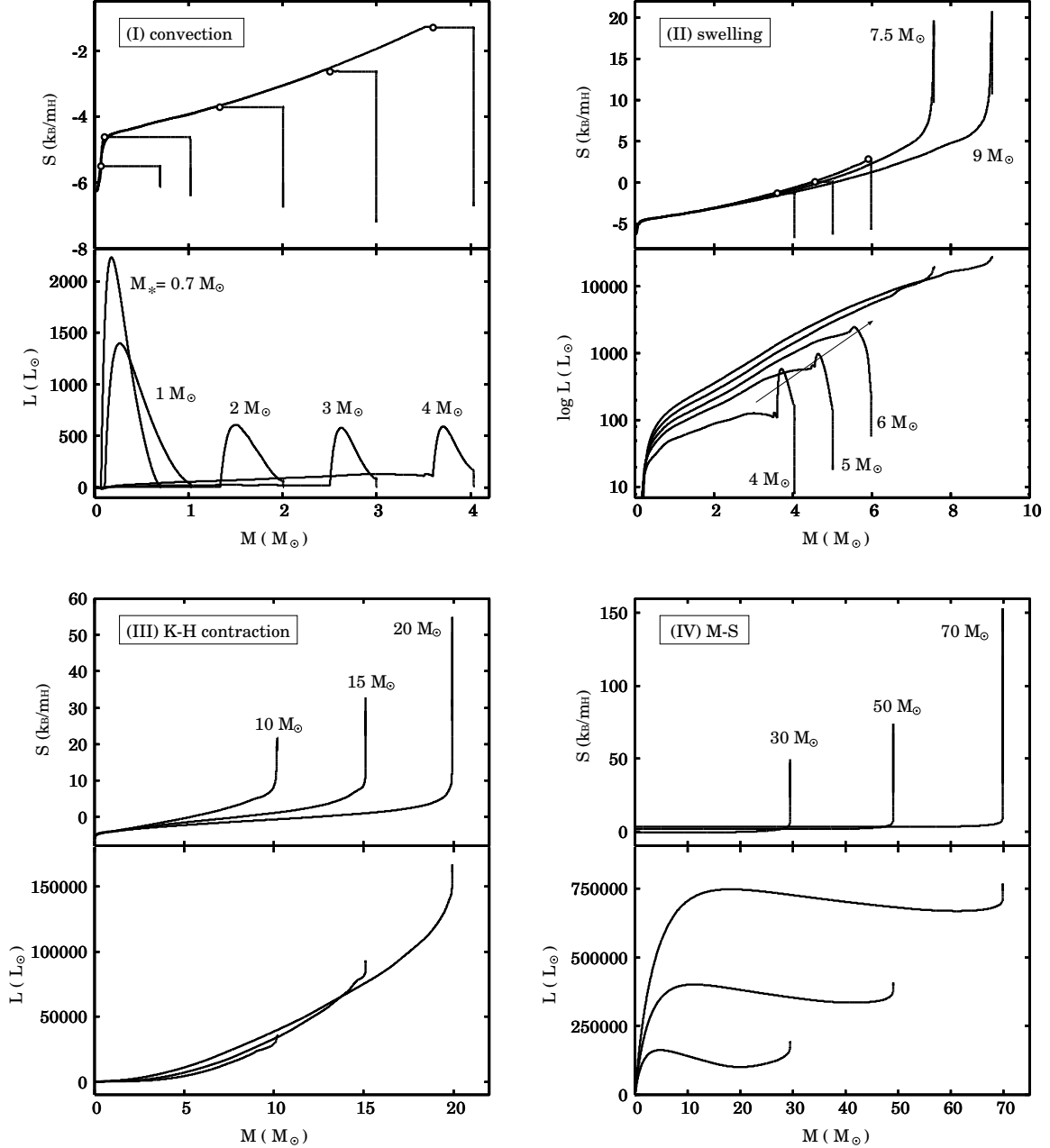


FIG. 6.— Radial profiles of the specific entropy and luminosity for disk accretion at the rate $\dot{M}_* = 10^{-3} M_\odot \text{ yr}^{-1}$ (case MD3-D). Illustration of the figure is the same as in Fig. 3. The four panels correspond to the four evolutionary phases, (I) convection (upper left), (II) swelling (upper right), (III) Kelvin-Helmholtz contraction (lower left), and (IV) main sequence accretion (lower right) phases. In the upper panels the open circles indicate the bottom edges of convective layers.

maximum radius.

We examine the mechanism of the swelling by considering the evolution after turning off deuterium burning. Figure 8 shows snapshots of entropy and luminosity profiles in each case. For $M_* \lesssim 8 M_\odot$ we find the characteristic feature of the “luminosity wave” in the luminosity profiles as in the spherical accretion case (see Section 3.1, and Fig. 3). The heat is transported from the interior where $\partial L / \partial M > 0$ to the surface layer where $\partial L / \partial M < 0$. The maximum luminosity increases with increasing stellar mass. At the same time the heat-losing interior extends outward toward the stellar surface. This characteristic evolution is caused by the decrease of opac-

ity within the star. More and more entropy embedded in the deep stellar interior is transferred outward by radiation as the opacity decreases. The surface layer bloats up, because it has a high entropy through absorbing part of the transported entropy. Figure 8 shows that the luminosity wave reaches the stellar surface for $M_* \simeq 9 M_\odot$. After that, $\partial L / \partial M > 0$ throughout the star and there is no entropy-receiving layer. However, the swelling still continues with disk accretion. This is because the newly accreted gas settles onto the star with the same high entropy of the stellar atmosphere. As a result, the surface layer always has high entropy. On the other hand, the stellar interior continues to lose entropy with decreasing

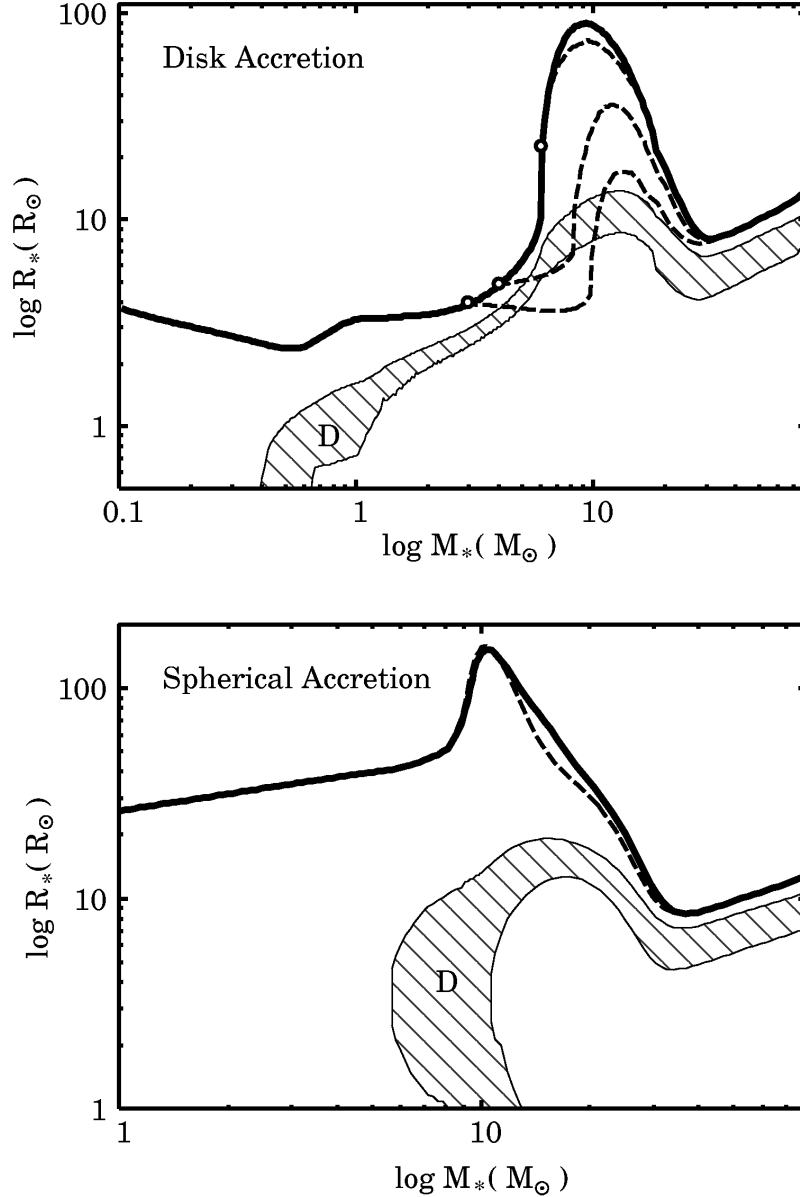


FIG. 7.— Effects of deuterium burning on protostellar evolution. The upper and lower panels show the evolution via disk and spherical accretion for $\dot{M}_* = 10^{-3} M_\odot \text{ yr}^{-1}$. In both panels the thick solid line represents the stellar radius. The hatched area denotes a layer with active deuterium burning, where the energy production rate is larger than $0.1 L_{\text{D, st}}/M_*$. In the upper panel the dashed lines show the evolution of the stellar radius after turning off deuterium burning at 3, 4, and $6 M_\odot$, respectively, which are indicated by open circles. In the lower panel the dashed line shows the evolution with no deuterium burning from the beginning.

opacity. The significant entropy loss in the stellar interior finally overcomes the swelling, and the star begins a phase of KH contraction.

Evolution of luminosity and entropy profiles with deuterium burning is shown in Figure 3. The evolution is qualitatively similar to that without deuterium burning presented in Figure 8. Deuterium burning increases the entropy within the star, which makes the heat transport after the opacity decreases more significant. Therefore, deuterium burning enhances the swelling. Figure 3 shows that with deuterium burning the luminosity wave reaches the surface when $M_* \simeq 6 M_\odot$. The stellar surface luminosity L_* significantly increases at this moment, which causes the inversion of the timescale balance (Fig. 5).

Later Phases— For $M_* \gtrsim 9 M_\odot$ the protostar begins to contract ($t_{\text{KH}} < t_{\text{acc}}$). The protostar efficiently loses its energy by radiation. Figure 6 shows that the entropy in the stellar interior decreases during this phase. The maximum temperature within the star soon exceeds 10^7 K. Hydrogen burning begins first via the pp-chain followed by CNO-cycle reactions, which lead to a convective core emerges when $M_* \simeq 20 M_\odot$. The stellar surface luminosity becomes nearly equal to the total energy production rate by CNO-cycle hydrogen burning for $M_* \simeq 30 M_\odot$ (Fig. 5). The stellar mass when the protostar reaches the ZAMS $M_{*, \text{ZAMS}}$ is analytically estimated by equating the accretion timescale to the KH timescale of ZAMS

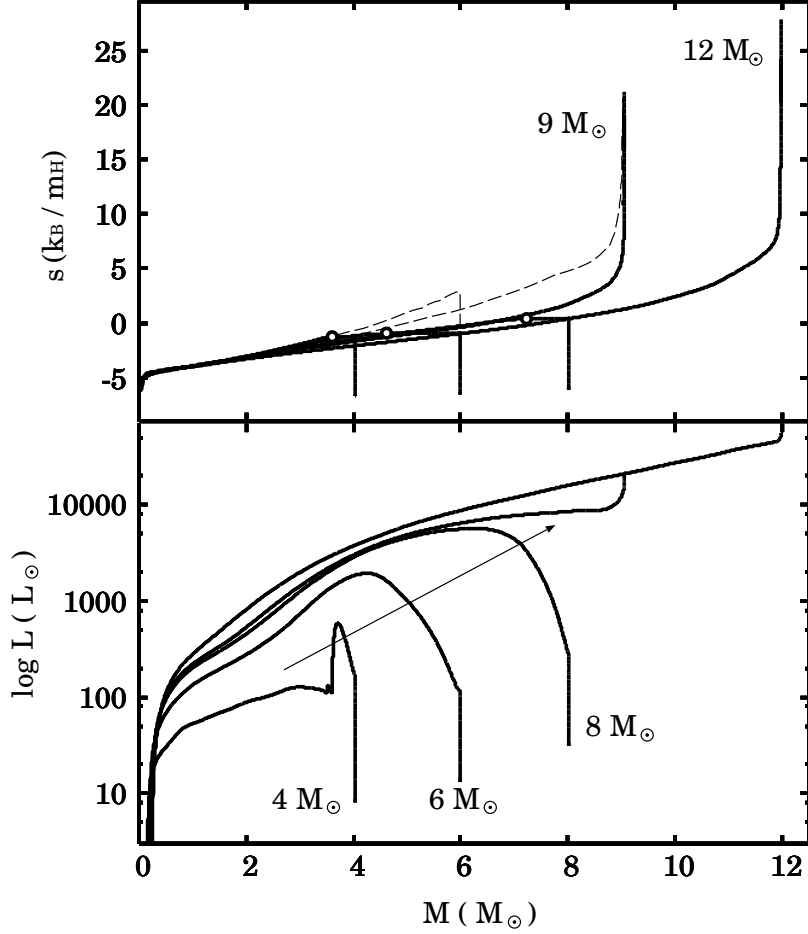


FIG. 8.— Evolution of radial profiles of specific entropy and luminosity after turning off deuterium burning at the point when $M_* = 4 M_\odot$. The lines labeled $4 M_\odot$ show the profiles just before turning off deuterium burning. The thin dashed lines in the upper panel show the entropy profiles for $M_* = 6 M_\odot$ and $9 M_\odot$ in the fiducial case with deuterium burning.

stars:

$$t_{\text{acc}} \simeq t_{\text{KH,ZAMS}}. \quad (12)$$

For $10 M_\odot \lesssim M_* \lesssim 100 M_\odot$ the mass-radius and mass-luminosity relationships of ZAMS stars (e.g. Schaller et al. 1992) are well fitted by:

$$L_{*,\text{ZAMS}} = 1.4 \times 10^4 L_\odot \left(\frac{M_*}{10 M_\odot} \right)^2, \quad (13)$$

$$R_{*,\text{ZAMS}} = 3.9 R_\odot \left(\frac{M_*}{10 M_\odot} \right)^{0.55}. \quad (14)$$

Substituting these relations into equation (12), we get

$$M_{*,\text{ZAMS}} \simeq 30.5 M_\odot \left(\frac{\dot{M}_*}{10^{-3} M_\odot \text{ yr}^{-1}} \right)^{0.645}, \quad (15)$$

which agrees well with our calculations. Since the above argument is independent of different accretion geometries, so is $M_{*,\text{ZAMS}}$.

3.2.2. Dependence on Initial Models

Next, we examine how the protostellar evolution changes with different initial models. To this end we

consider two initial models that differ from the the fiducial one. One is a $0.1 M_\odot$ star with a shallower initial entropy distribution ($\beta = 0.1$ in equation (7); case MD3-D-b0.1). The other is a fully convective $1.3 M_\odot$ star (case MD3-D-cv), which was used by Palla & Stahler (1992) to calculate the evolution at $\dot{M}_* = 10^{-4} M_\odot \text{ yr}^{-1}$ via cold disk accretion. Figure 9 shows the evolution of stellar radius and maximum temperature in these cases. The basic evolution is similar. A protostar undergoes swelling and contraction, finally reaching the main sequence accretion phase when $M_* \simeq 30 M_\odot$. However, the evolution differs quantitatively for the different initial models. For example the maximum stellar radius is $\simeq 400 R_\odot$ for case MD3-D-b0.1, but $\simeq 30 R_\odot$ for case MD3-D-cv (the evolution of the interior structure in these cases also differs slightly from that for case MD3-D described in Section 3.2; see Appendix A for details).

This is in stark contrast to the spherical accretion case, where the evolution is almost independent of different initial models. For spherically symmetric accretion the evolution of stellar radius in the adiabatic accretion phase is well approximated by the relation (Stahler, Palla &

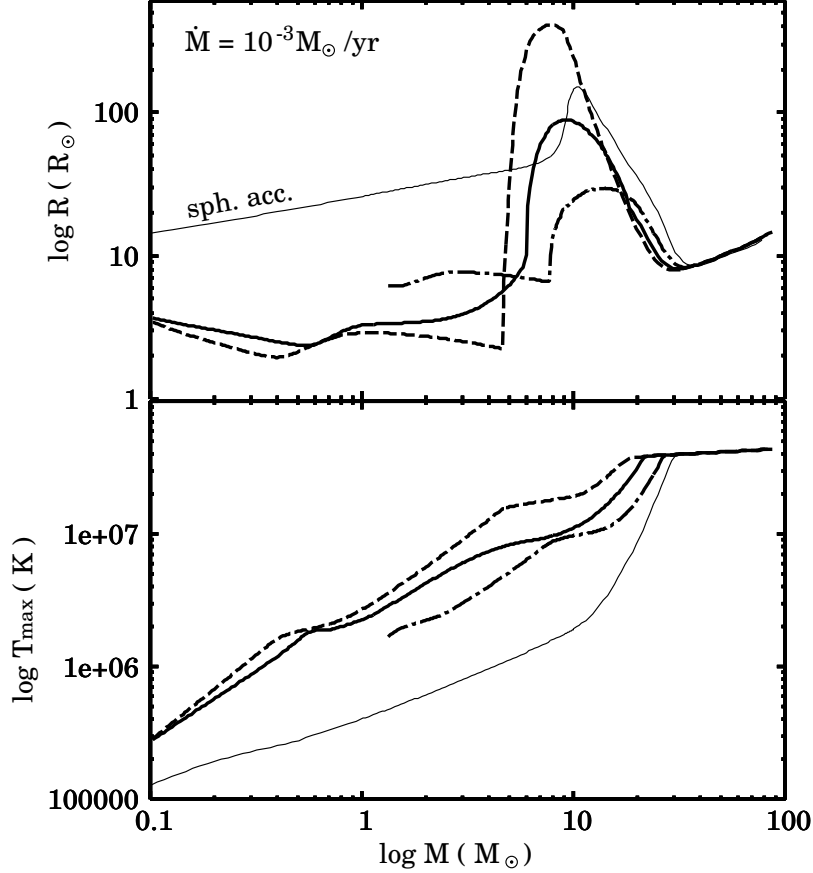


FIG. 9.— Variation of evolution via disk accretion with different initial models with an adopted accretion rate $\dot{M}_* = 10^{-3} M_\odot \text{ yr}^{-1}$. The upper and lower panels display the evolution of the protostellar radius and maximum temperature within the star. In both panels the solid line shows the evolution in the fiducial case explained in Section 3.2.1 (case MD3-D), the dashed line represents the evolution assuming a shallower initial entropy distribution (case MD3-D-b0.1), and the dot-dashed line shows the evolution with a fully convective initial model (case MD3-cv). For comparison we also display the evolution for spherical accretion at the same accretion rate (case MD3-S) with a thin solid line.

Salpeter 1986):

$$R_* \simeq 26 R_\odot \left(\frac{M_*}{M_\odot} \right)^{0.27} \left(\frac{\dot{M}_*}{10^{-3} M_\odot \text{ yr}^{-1}} \right)^{0.41}. \quad (16)$$

Our calculated evolution with spherical accretion (case MD3-S) also obeys this relation before the swelling occurs. Stahler, Palla & Salpeter (1986) showed that the evolution of the radius converges to the above relation even beginning with different initial models. With spherical accretion entropy generated at an accretion shock front is taken into the stellar interior along with the accreted gas. If the initial radius is too large compared to equation (16), the accretion shock front is weak due to the shallow gravitational potential well. The entropy produced at the accretion shock front is reduced, which decreases average entropy within the star. As a result the protostar contracts. If the initial radius is too small, the opposite occurs, increasing the radius. With disk accretion, however, this regulation process does not operate. The entropy of the accreted material is set to the value in the stellar atmosphere. Since the structure of the stellar atmosphere differs with different initial models, the subsequent evolution also changes (also see Hartmann et al. 1997 for low-mass protostars).

How should we choose the initial model? We infer this

by considering the evolution of accretion flow toward the protostar. Just after a protostar is born, the protostar gathers material from its immediate vicinity with low angular momentum. The geometry of the accretion flow is nearly spherical in this early phase. Afterwards, gas originally far from the star falls toward the star with increasingly higher angular momentum. A circumstellar disk forms, and the protostar continues to grow via disk accretion. The protostellar evolution in this scenario is calculated by switching the accretion geometry from spherical to disk accretion at some point.

Figure 10 shows some examples of protostellar evolution, whereby the accretion geometry is switched for $M_* = 0.1 M_\odot$ and $1 M_\odot$. The protostellar radius increases in the early spherical accretion phase according to equation (16). The radius subsequently decreases after the geometry is switched to cold disk accretion, because the accreting gas brings lower entropy into the stellar interior. The interior temperature increases as the protostar contracts. Active deuterium burning begins when the maximum temperature exceeds $\simeq 10^6$ K. Figure 10 shows that, the earlier the geometry is switched, the earlier deuterium burning begins. The subsequent evolution is similar to that in our fiducial case MD3-D explained in Section 3.2. The maximum radius is $\simeq 50 R_\odot$ in both examined cases. The protostar reaches the main sequence accretion phase at $M_* \simeq 30 M_\odot$, which is independent

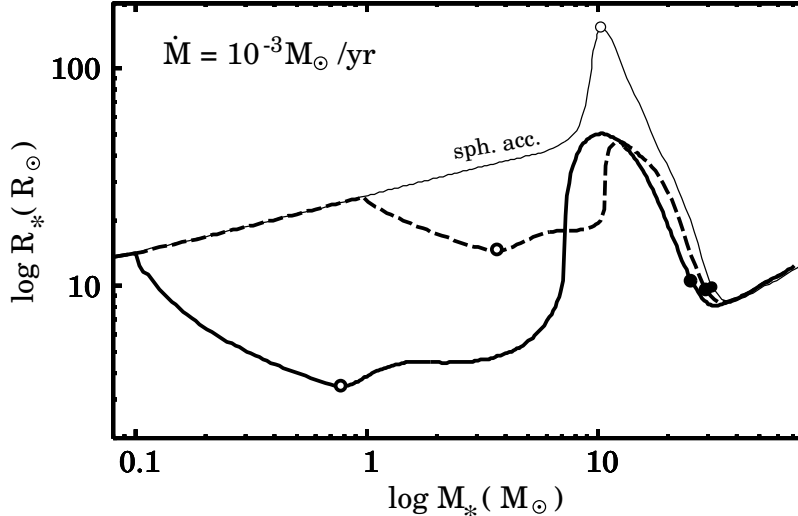


FIG. 10.— Evolution of the stellar radius when the accretion geometry is switched from spherical accretion to disk accretion at a constant rate $\dot{M}_* = 10^{-3} M_\odot \text{ yr}^{-1}$. The thick solid and dashed lines show the evolution when the geometry is changed at $M_* = 0.1 M_\odot$ and $1 M_\odot$ (cases MD3-SDm0.1 and MD3-SDm1), respectively. The open circles mark the epoch when the total energy production rate by deuterium burning reaches 80% of the steady burning rate $L_{D,st}$. The filled circles indicate the epoch when the total energy production rate by hydrogen burning exceeds 80% of the luminosity at the stellar surface L_* . The thin line shows the evolution assuming spherical accretion only (case MD3-S).

of the history of accretion geometry.

3.3. Comparison with Primordial Protostars

Rapid mass accretion $\dot{M}_* \sim 10^{-3} M_\odot \text{ yr}^{-1}$ is also expected during the formation of primordial ($Z = 0$) stars. Here, we compare the evolution of primordial protostars to that of present-day ($Z = Z_\odot$) massive protostars. Figure 11 presents the evolution of the stellar radius with metallicities $Z = 0$ (case MD3-SDm0.1-z0) and $Z = Z_\odot$ (case MD3-SDm0.1). In these cases the accretion geometry is switched from spherical accretion to disk accretion at $M_* = 0.1 M_\odot$. The basic evolution with $Z = 0$ is the same as in the present-day case. After deuterium burning begins for $M_* \simeq 0.8 M_\odot$, the protostar undergoes the four evolutionary phases of convection, swelling, KH contraction, and main sequence accretion.

However, Figure 11 also shows some quantitative differences between the primordial and present-day cases. At $Z = 0$, for example, the swelling occurs for $M_* \simeq 6 M_\odot$, which is slightly earlier than for solar metallicities. A similar difference is also found with spherical accretion, as shown in Figure 11. These differences are attributed to the fact that the opacity is lower at lower metallicity in the same thermal state. As explained in Section 3.1 and 3.2, the swelling occurs as a result of the decrease of opacity in the stellar interior with increasing the stellar mass. The swelling occurs earlier at $Z = 0$, because the opacity decreases sufficiently at an earlier time.

Another difference between the primordial and present-day case is the stellar radius in the main sequence accretion phase; the ZAMS radius for $Z = 0$ is much smaller than that for $Z = Z_\odot$, independent of the assumed geometry. In the primordial case the initial abundance of C, N, and O nuclei, necessary catalysts for the CNO-cycle hydrogen burning, is zero. CNO-cycle reactions do not begin until these atoms are provided by helium triple- α burning, which occurs at $T \simeq 10^8 \text{ K}$.

Because pp-chain hydrogen burning does not supply sufficient energy to halt the star's KH contraction, the pre-main contraction phase continues up to the higher central densities and temperatures that allow triple- α reactions. This ZAMS star thus has a much smaller radius than its solar metallicity counterpart.

4. DEPENDENCE ON MASS ACCRETION RATES

Finally, we examine how the protostellar evolution changes with different accretion rates. As pointed out in Section 3.2.2, the evolution quantitatively varies with different initial models even at the same accretion rate. In this section we focus on the cases where the accretion geometry evolves from spherical accretion to disk accretion in early phases. Figure 12 displays the evolution of the stellar radius at the accretion rates of $\dot{M}_* = 10^{-4} M_\odot \text{ yr}^{-1}$ (case MD4-SDm0.1), $10^{-3} M_\odot \text{ yr}^{-1}$ (case MD3-SDm0.1), and $4 \times 10^{-3} M_\odot \text{ yr}^{-1}$ (case MD4x3-SDm0.5). With the rate $10^{-4} M_\odot \text{ yr}^{-1}$, the protostar undergoes the same four evolutionary phases as with the rate $10^{-3} M_\odot \text{ yr}^{-1}$. The maximum radius decreases with decreasing the accretion rate. The same dependence is also seen with spherical accretion. Note that, however, the maximum radius varies with different initial models under the assumption of a freely radiating photospheric boundary ("disk accretion") as explained in Section 3.2.2. Figure 12 also shows that, at lower accretion rates, the protostar arrives to the main-sequence accretion phase at a lower stellar mass. We argue that this dependence is robust. The stellar mass at the arrival to the ZAMS is just determined by $t_{acc} \simeq t_{KH,ZAMS}$ as shown by equation (15), which is independent of different accretion geometries and different initial models.

Figure 12 shows a qualitatively different evolution at the higher rate $\dot{M}_* = 4 \times 10^{-3} M_\odot \text{ yr}^{-1}$. With spherical accretion a period of rapid expansion occurs when $M_* \simeq 50 M_\odot$. This expansion was originally found by

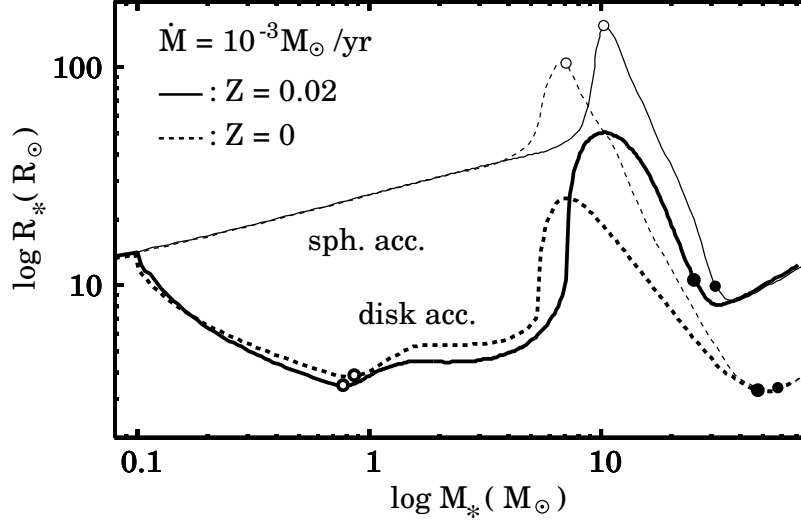


FIG. 11.— Comparison with primordial cases: Evolution of protostellar radius for an accretion rate $\dot{M} = 10^{-3} M_{\odot} \text{ yr}^{-1}$. The thick solid and dotted lines show the evolution via disk accretion at $Z = 0.02$ (case MD3-SDm0.1) and $Z = 0$ (case MD3-SDm0.1-z0), respectively. The accretion geometry was switched from spherical accretion to disk accretion when $M_* = 0.1 M_{\odot}$. The thin solid and dashed lines show the corresponding evolution via spherical accretion for each metallicity (cases MD3-S and MD3-S-z0). The meanings of the open and filled circles on the curves are the same as in Figure 10.

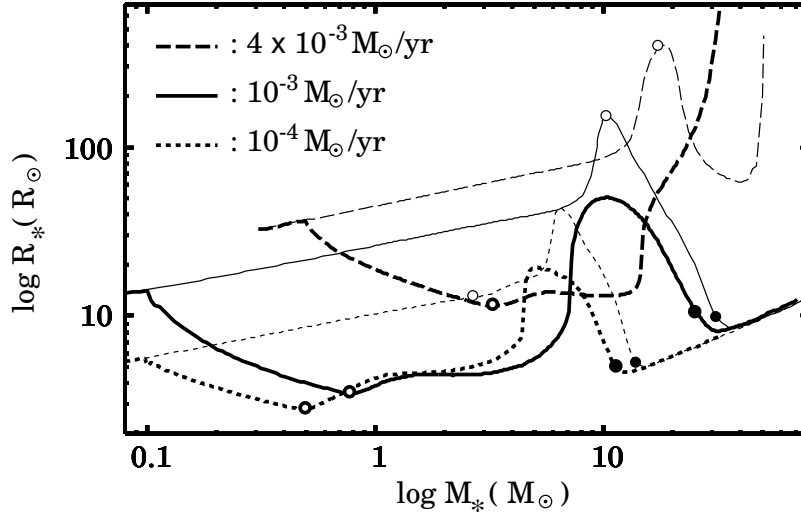


FIG. 12.— Evolution of the protostellar radius with disk accretion at different accretion rates $\dot{M} = 10^{-4} M_{\odot} \text{ yr}^{-1}$ (case MD4-SDm0.1, dotted line), $10^{-3} M_{\odot} \text{ yr}^{-1}$ (case MD3-SDm0.1, solid line), and $4 \times 10^{-3} M_{\odot} \text{ yr}^{-1}$ (case MD4x3-SDm0.5, dashed line). The evolution with spherical accretion at each rate is also plotted with thin lines for comparison (cases MD4-S, MD3-S, and MD4x3-S). The meanings of the open and filled circles on the curves are the same as in Figure 10.

Omukai & Palla (2001, 2003) at zero metallicity. The expansion occurs when the total luminosity L_{tot} approaches the Eddington luminosity, where $L_{\text{tot}} = L_* + L_{\text{acc}}$ and L_{acc} is an additional component from the accretion shock front, $L_{\text{acc}} = GM_*\dot{M}_*/R_*$. In Paper I, we showed that the critical Eddington ratio $L_{\text{tot}}/L_{\text{Edd}}$, above which the expansion occurs, is about 0.5 at $Z = Z_{\odot}$ (presented again in Figure 13). The critical ratio less than unity is because the opacity near the stellar surface is somewhat higher than the electron-scattering opacity.

When L_{tot} reaches $0.5L_{\text{Edd}}$ in the KH contraction phase, rapid expansion occurs and inhibits growth of

the protostar by steady mass accretion. We can derive the critical accretion rate $\dot{M}_{*,\text{cr}}$, with which the protostar barely reaches the ZAMS without undergoing rapid expansion, from the critical Eddington ratio as follows (Omukai & Palla 2003; Paper I). In the critical case, L_{tot} reaches $0.5L_{\text{Edd}}$ when the protostar arrives to the ZAMS. Thus, in the spherical accretion case, the critical rate $\dot{M}_{*,\text{cr}}$ satisfies the relation

$$L_{\text{ZAMS}} + \frac{GM_{\text{ZAMS}}\dot{M}_{*,\text{cr}}}{R_{\text{ZAMS}}} = 0.5L_{\text{Edd}}, \quad (17)$$

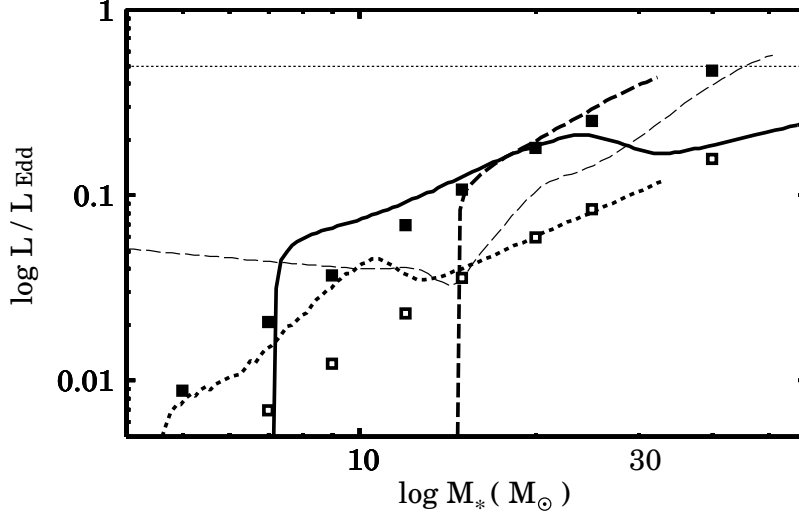


FIG. 13.— Evolution of Eddington ratio of protostars with disk accretion. The dotted, solid, and dashed lines represent L_*/L_{Edd} for the different accretion rates $\dot{M}_* = 10^{-4} M_\odot \text{ yr}^{-1}$ (case MD4-SDm0.1), $10^{-3} M_\odot \text{ yr}^{-1}$ (case MD3-SDm0.1), and $4 \times 10^{-3} M_\odot \text{ yr}^{-1}$ (case MD4x3-SDm0.5), respectively. The thin dashed line shows the evolution of $L_{\text{tot}}/L_{\text{Edd}}$ for spherical accretion with $4 \times 10^{-3} M_\odot \text{ yr}^{-1}$ (case MD4x3-S) for comparison, whereby $L_{\text{tot}} = L_* + GM_*\dot{M}_*/R_*$. The thin dotted line indicates the critical ratio $L/L_{\text{Edd}} = 0.5$. The open squares show the luminosity of ZAMS stars $L_{\text{ZAMS}}(M_*)$ calculated by Schaller et al. (1992). The filled squares show $3 \times L_{\text{ZAMS}}(M_*)$.

where the suffix “ZAMS” indicates the quantities of ZAMS stars. This relation is transformed to

$$\dot{M}_{*,\text{cr}} = \frac{4\pi c R_{\text{ZAMS}}}{\kappa_{\text{esc}}} \left(1 - \frac{L_{\text{ZAMS}}}{0.5 L_{\text{Edd}}} \right), \quad (18)$$

where κ_{esc} is the electron-scattering opacity, a lower limit to the actual opacity. The critical rate given by this equation is a function of M_* , but its dependence is weak. The numerical value is $\dot{M}_{*,\text{cr}} \simeq 3 \times 10^{-3} M_\odot \text{ yr}^{-1}$ over a wide range of M_* , which is consistent with our numerical results.

We see that a similar expansion also occurs for $4 \times 10^{-3} M_\odot \text{ yr}^{-1}$ in the cold disk accretion limit in Figure 12. In this case the protostar very abruptly inflates when $M_* \gtrsim 20 M_\odot$ and never turns to KH contraction. The stellar radius finally exceeds $600 R_\odot$ for $M_* \simeq 30 M_\odot$. YB08 also reported a similar evolution for the accretion rate $10^{-2} M_\odot \text{ yr}^{-1}$. Interestingly, it is known that a similar expansion also occurs when a main-sequence star undergoes rapid mass accretion due to mass exchange in close binary systems. Kippenhahn & Mayer-Hofmeister (1977) and Neo et al. (1977) considered the accretion of deuterium-free gas onto existing main sequence stars. The numerical method they adopted is basically the same as ours; the protostellar structure was numerically calculated with a freely radiating photospheric boundary condition.

Figure 13 shows that the critical Eddington ratio for the expansion is also $L_*/L_{\text{Edd}} \simeq 0.5$ in the cold disk accretion limit. Note that there is no additional luminosity component L_{acc} here. The accretion luminosity is assumed to have already radiated into free space before the accreted material settles onto the star. The critical accretion rate in this case is derived as follows. As explained in Section 3.2, the stellar luminosity L_* significantly rises in the swelling phase. The luminosity comes from release of gravitational energy after that. Figure 13 shows that the stellar luminosity in this phase roughly

follows

$$L_* \simeq 3 \times L_{\text{ZAMS}}(M_*) \quad (19)$$

in all cases considered. The stellar luminosity approaches $L_{\text{ZAMS}}(M_*)$ just before the arrival to the ZAMS at the rate 10^{-4} and $10^{-3} M_\odot \text{ yr}^{-1}$. At the rate $4 \times 10^{-3} M_\odot \text{ yr}^{-1}$, however, L_* approaches $0.5 L_{\text{Edd}}$ before reaching the ZAMS and the abrupt expansion occurs. The stellar mass at which $L_* \simeq 0.5 L_{\text{Edd}}$ is $M_* \simeq 45 M_\odot$ using equation (19). In order to avoid expansion the protostar has to reach the ZAMS with a mass $M_{*,\text{ZAMS}} \lesssim 45 M_\odot$. This condition is transformed to that for accretion rates with equation (15),

$$\dot{M} \lesssim \dot{M}_{*,\text{cr}} \simeq 2 \times 10^{-3} M_\odot \text{ yr}^{-1}. \quad (20)$$

The derived critical rate is comparable to that for spherically symmetric accretion, as confirmed by our numerical calculations.

Our calculations suggest that a massive protostar significantly bloats up and can not reach the ZAMS by steady mass accretion, if the accretion rate is higher than a few $10^{-3} M_\odot \text{ yr}^{-1}$. This feature is independent of the accretion geometry. If mass accretion completely shuts off as a result of the fast expansion of the protostar, there will be an upper mass limit of pre-main-sequence stars around several $10s M_\odot$, as discussed in Paper I. Otherwise, mass accretion might continue in a non-steady fashion. At least, it is certain that the radius of a massive protostar reaches several $100s R_\odot$ at the high accretion rate. The very large radius leads to a low effective temperature of the protostar.

For case MD4x3-SDm0.5, for example, the stellar luminosity exceeds $10^5 L_\odot$ for $M_* \gtrsim 18 M_\odot$, but the effective temperature is only $T_{\text{eff}} \lesssim 10^4 \text{ K}$, the value of a $M_* \lesssim 2.5 M_\odot$ ZAMS star. The stellar UV luminosity is very low for such low T_{eff} . This is important for the growth of an H II region around the protostar (e.g., Hoare & Franco 2007). Observationally, High-Mass Protostel-

lar Objects (HMPOs) are considered to be young forming massive stars prior to the formation of an H II region. However, a lot of HMPOs have high infrared luminosity exceeding $10^4 L_{\odot}$ without observable H II regions (e.g., Sridharan et al. 2002; Beltrán et al. 2006b; Beuther et al. 2007). There has been some speculation regarding what hinders the growth of H II regions around these bright sources. ZAMS stars with such high luminosity should ionize their surroundings. Some authors have proposed that rapid mass accretion quenches the growth of H II regions by increasing the gas density and recombination rate near the protostar (e.g., Walmsley 1995). With disk accretion, however, the H II region would break out in the polar direction, where the gas density decreases significantly after the material with low angular momentum has accreted onto the star or been expelled in an outflow.

Our calculations well explain the existence of such bright HMPOs even with disk accretion. Massive stars accreting at high rates bloat up; their UV luminosity is too low to form the H II region.

5. SUMMARY AND CONCLUSIONS

In this paper we have studied the evolution of massive protostars with disk accretion at high rates $\dot{M}_* > 10^{-4} M_{\odot} \text{ yr}^{-1}$. We considered the limiting case of “cold” disk accretion, whereby most of the stellar surface is not affected by the accretion flow, and the accreting material brings a minimum of entropy into the star. We calculated the evolution of protostars in this limiting case by adopting the photospheric (freely radiating) boundary condition. The calculated evolution was compared and contrasted to the evolution with spherically symmetric accretion, corresponding to the opposite limit, whereby the accreting gas transports the maximum amount of entropy into the star.

First, we considered in detail the evolution for $\dot{M}_* = 10^{-3} M_{\odot} \text{ yr}^{-1}$. The basic evolution via the cold disk accretion is summarized as follows:

The entire evolution is divided into four evolutionary phases: (I) convection, (II) swelling, (III) KH contraction, and (IV) the main-sequence accretion phase. The evolution in the first three phases varies with different initial models. Roughly speaking, the stellar radius reaches its maximum $30 - 400 R_{\odot}$ for $M_* \simeq 10 M_{\odot}$ at the end of the swelling phase (II). On the other hand, the protostar begins the final phase (IV) for $M_* \simeq 30 M_{\odot}$, independent of different initial models.

A key physical quantity governing the evolution is the opacity in the stellar interior, analogous to the spherical accretion case. The opacity decreases with increasing stellar mass, which causes the variety of the evolution. In phase (I) the opacity is so high that the radiative heat transport within the star does not affect the stellar structure. In phase (II) the entropy accumulated in the stellar interior is gradually transported outward as the opacity decreases. A part of the transported entropy is received in a thin layer near the stellar surface. Due to the high

entropy deposited into this layer it significantly bloats up, resulting in the swelling seen in phase (II). Afterwards, the opacity decreases sufficiently, allowing the star to lose heat by efficiently radiation. The protostar contracts and the interior densities and temperatures rise. This is the KH contraction phase (III). The protostar finally reaches the main-sequence accretion phase (IV), just after the active hydrogen burning begins.

A major difference between the results for spherical accretion and cold disk accretion is the role of deuterium burning. In the limit of cold disk accretion the accreting gas brings a minimal amount of entropy into the star. Since the stellar radius is smaller because of the lower average entropy in the stellar interior, the protostellar radius is initially small, $R_* \simeq \text{a few} \times R_{\odot}$. However, deuterium burning begins earlier, which raises the entropy content within the star. This enhances the swelling. Consequently, the maximum radius is as large as that with spherical accretion.

Next, we calculated the protostellar evolution at zero metallicity in the cold disk accretion limit. The protostellar evolution varies with metallicities in the same manner as with spherical accretion; at $Z = 0$, the protostar swells up slightly earlier, and reaches the ZAMS with a smaller stellar radius.

Finally, we examined the evolution with different accretion rates. Our calculations show some dependences on accretion rates which were also found with spherical accretion. First, the stellar mass at the arrival to the ZAMS is higher for higher accretion rates. However, if the accretion rate is higher than a few $10^{-3} M_{\odot} \text{ yr}^{-1}$, the stellar radius continues to increase without returning to KH contraction. The protostar never reaches the ZAMS by steady mass accretion at such high rates.

The fact that a massive protostar bloats up to a radius of several $100s R_{\odot}$ with an accretion rate exceeding $10^{-3} M_{\odot} \text{ yr}^{-1}$ is a very robust result of our studies. The large radius leads to a low effective temperature and a correspondingly low stellar UV luminosity. Thus, the growth of an H II region will be delayed until mass accretion onto the star ceases significantly. This explains the existence of HMPOs with high luminosities exceeding $10^4 L_{\odot}$.

We thank Peter Bodenheimer for a careful critique of the manuscript. We also thank Neal Turner for fruitful comments and discussions. This study is supported in part by Research Fellowships of the Japan Society for the Promotion of Science for Young Scientists (TH) and by the Grants-in-Aid by the Ministry of Education, Science and Culture of Japan (18740117, 18026008, 19047004: KO). Portions of this work were conducted at the Jet Propulsion Laboratory, California Institute of Technology, operating under a contract with the National Aeronautics and Space Administration (NASA).

REFERENCES

- Beech, M. & Mitalas, R., 1994, *ApJS*, 95, 517
- Behrend, R. & Maeder, A., 2001, *A&A*, 373, 190
- Beltrán, M.T., Cesaroni, R., Codella, C., Testi, L., Furuya, R.S. & Olmi, L., 2006, *Nature*, 443, 427
- Beltrán, M.T., Brand, J., Cesaroni, R., Fontani, F., Pezzuto, S., Testi, L. & Molinari, S., 2006, *A&A*, 447, 221
- Beuther, H., Zhang, Q., Hunter, T.R., Sridharan, T.K. & Bergin, E.A., 2007, *A&A*, 473, 493

- Bodenheimer, P., Laughlin, G.P., Rozyczka, M. & Yorke, H.W., 2007, *Numerical Methods in Astrophysics: An Introduction.*, (New York: Taylor & Francis)
- Bonnell, I.A., Bate, M.R. & Zinnecker, H., 1998, MNRAS, 298, 93
- Bonnell, I.A., Vine, S.G. & Bate, M.R., 2004, MNRAS, 349, 735
- Bontemps, S., Motte, F., Csengeri, T. & Schneider, N., 2010, astro-ph/0909.2315
- Cesaroni, R., Galli, D., Lodato, G., Walmsley, C. M., Zhang, Q., 2007, in *Protostars and Planets V*, eds. B.Reipurth, D.Jewitt, & K.Keil (Tucson: Univ. Arizona Pres), 197
- Cox, J.P. & Giuli, R.T., 1968, *Principles of Stellar Structure.*, Gordon & Breach, New York
- Furuya, R.S. & Shinnaga, H., 2009, ApJ, 703, 1198
- Hartmann, L., Cassen, P. & Kenyon, S.J., 1997, ApJ, 475, 770
- Hoare, M.G. & Franco, J. 2007, in *Diffuse Matter from Star Forming Regions to Active Galaxies*, ed. T.W. Hartquist, J.M. Pittard, & S.A.E.G. Falle (Dordrecht: Springer), 61
- Hosokawa, T. & Omukai, K., 2008, in *Astronomical Society of the Pacific Conference Series*, Vol. 387, ed. H.Beuther, H.Linz & T.Henning, p255
- Hosokawa, T. & Omukai, K., 2009a, ApJ, 691, 823 (Paper I)
- Hosokawa, T. & Omukai, K., 2009b, ApJ, 703, 1810
- Kippenhahn, R. & Meyer-Hofmeister, E., 1977, A&A, 54, 539
- Krumholz, M.R., Klein, R.I. & McKee, C.F., 2007, ApJ, 656, 959
- Krumholz, M.R., Klein, R.I., McKee, C.F., Offner, S.S.R. & Cunningham, A.J., 2009, Science, 323, 754
- Larson, R.B. & Starrfield, S. 1971, A&A, 13, 190
- Marseille, M., Bontemps, S., Herpin, F., van der Tak, F.F.S., & Purcell, C.R., 2008, A&A, 488, 579
- McKee, C.F. & Tan, J.C., 2002, Nature, 416, 59
- McKee, C.F. & Tan, J.C., 2003, ApJ, 585, 850
- Morino, J., Yamashita, T., Hasegawa, T. & Nakano, T., 1998, Nature, 393, 340
- Motte, F., Bontemps, S., Schilke, P., Schneider, N., Menten, K.M. & Brogiere, D., 2007, A&A, 476, 1243
- Neo, S., Miyaji, S., Nomoto, K. & Sugimoto, D., 1977, PASJ, 29, 249
- Norberg, P. & Maeder, A., 2000, A&A, 359, 1025
- Omukai, K. & Palla, F., 2001, ApJ, 561, 550L
- Omukai, K. & Palla, F., 2003, ApJ, 589, 677
- Palla, F. & Stahler, S.W., 1991, ApJ, 375, 288
- Palla, F. & Stahler, S.W., 1992, ApJ, 392, 667
- Palla, F., Salpeter, E.E. & Stahler, S.W., 1983, ApJ, 271, 632
- Patel, N.A. et al., 2005, Nature, 437, 109
- Schaller, G., Schaerer, D., Meynet, G. & Maeder, A., 1992, A&AS, 96, 269
- Sridharan, T.K., Beuther, H., Schilke, P., Menten, K.M. & Wyrowski, F., 2002, ApJ, 566, 931
- Stacy, A., Grief, T.H. & Bromm, V., 2010, MNRAS
- Stahler, S.W., Palla, F. & Salpeter, E.E., 1986, ApJ, 302, 590
- Stahler, S.W., Shu, F.H. & Taam, R.E., 1980, ApJ, 242, 226
- Tan, J.C. & McKee, C.F., 2004, ApJ, 603, 383
- Walmsley, C.M., 1995, Rev. Mex. Ast. Ap. Conf. Ser. 1, 137
- Wang, P., Li, Z.Y., Abel, T. & Nakamura, F., 2009, astro-ph/0908.4129
- Wolfire, M.G. & Cassinelli, J.P., 1987, ApJ, 319, 850
- Yorke, H.W. & Bodenheimer, P., 2008, in *Astronomical Society of the Pacific Conference Series*, Vol. 387, ed. H.Beuther, H.Linz & T.Henning, p189 (YB08)
- Yorke, H.W. & Sonnhalter, C., 2002, ApJ, 569, 846
- Yoshida, N., Omukai, K. & Hernquist, L., 2008, Science, 321, 669
- Zhang, Q., Wang, Y., Pillai, T. & Rathborne, J., 2009, ApJ, 696, 268
- Zinnecker, H. & Yorke, H.W., 2007, ARA&A, 45, 481

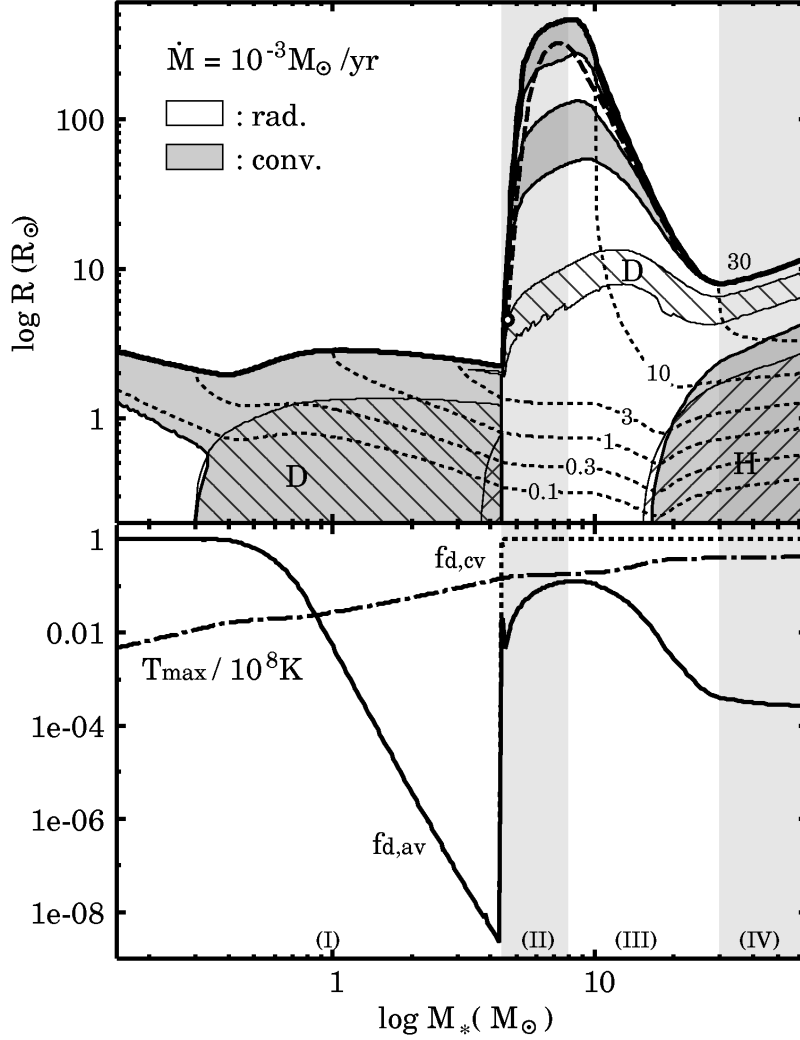


FIG. A1.— Same as Fig.4 but for a different initial model with a shallower entropy distribution (case MD3-D-b0.1). In the upper panel the dashed line shows the evolution of stellar radius after deuterium burning is turned off at the point marked by the open circle.

APPENDIX

A. EVOLUTION FOR $\dot{M}_* = 10^{-3} M_\odot \text{ yr}^{-1}$ WITH SHALLOW INITIAL ENTROPY PROFILE

In Section 3.2.2, we have seen that the protostellar evolution differs with different initial models under the cold disk accretion even at the same accretion rate. In this appendix, we add a more detailed explanation of these differences. We revisit case MD3-D-b0.1 (Section 3.2.2), whereby the initial entropy distribution is shallower than for the fiducial case MD3-D. The principle difference occurs in the first convection phase (I) (see Figure A1). A central convective core emerges soon after the onset of deuterium burning when $M_* \simeq 0.3 M_\odot$. The convective core grows outward and merges with the outer convective layer near the surface: The protostar becomes fully convective for $M_* \simeq 0.4 M_\odot$. This is not seen in case MD3-D, where the core remains radiative even after D-burning begins.

The subsequent evolution also differs. For case MD3-D (see Figure 4) the radiative core gradually extends outward with increasing the stellar mass. The D-burning layer, located at the bottom of the outer convective layer, also moves outward, until the protostar swells up ($M_* \simeq 6 M_\odot$). For case MD3-D-b0.1, on the other hand, deuterium burning continues at the stellar center as long as the protostar remains fully convective and freshly accreted gas (containing deuterium) is mixed downward. The deuterium is significantly depleted in this fully convective phase (lower panel of Fig. A1). When $M_* \simeq 5 M_\odot$ a thin radiative layer (a so-called “radiative barrier”) forms within the star, and the stellar structure changes significantly. This radiative barrier blocks the convective transport of newly accreted deuterium into the stellar interior. Without the refurbishment of deuterium, the central zones quickly consume all available deuterium and become radiative. Deuterium burning continues in a thin layer outside the radiative core.

The evolution described above is similar to that of intermediate-mass protostars as calculated by Palla & Stahler (1991, 1992; also see Appendix B.1 below). The significant heat input by the deuterium shell-burning triggers the rapid swelling of the star. The stellar radius ultimately expands to about $400 R_\odot$. As in case MD3-D, however, deuterium

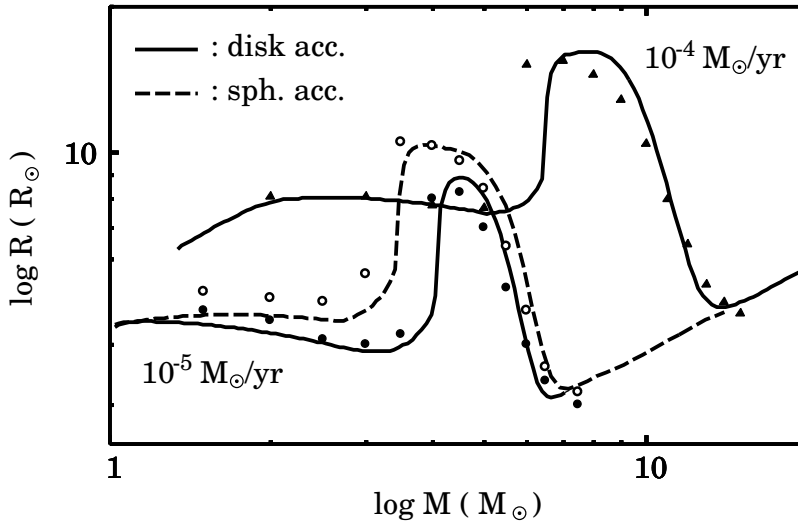


FIG. B1.— Comparison with Palla & Stahler (1992): The evolution of protostellar radius for our calculations (lines) and Palla & Stahler's (symbols). The dashed line and open circles represent the evolution via spherical accretion for $10^{-5} M_{\odot} \text{yr}^{-1}$ (case MD5-S-cv). The evolution via disk accretion for 10^{-5} & $10^{-4} M_{\odot} \text{yr}^{-1}$ (cases MD5 & MD4-D-cv) is depicted by the lower & upper solid line and the filled circles & triangles, respectively. The initial models were constructed following Palla & Stahler (1992).

shell-burning per se is not the main driver of the swelling. Figure A1 shows that, even if we turn off D-burning just after the swelling begins, the protostar continues to swell up. The protostar expands because a thin surface layer bloats up after receiving entropy transported from the inner part of the star.

B. COMPARISON WITH PREVIOUS WORK

B.1. Comparison with Palla & Stahler (1992)

We compare our numerical results with previous calculations by Palla & Stahler (1992), who studied protostellar evolution in the limit of cold disk accretion with accretion rates $10^{-5} M_{\odot} \text{yr}^{-1}$ and $10^{-4} M_{\odot} \text{yr}^{-1}$. The numerical method adopted by Palla & Stahler (1992) is the same as ours (e.g., Stahler, Shu & Taam 1980). The same photospheric boundary condition (equations 2 and 3) was used for the limiting case of cold disk accretion. The initial models they adopted are $1.0 M_{\odot}$ and $1.3 M_{\odot}$ fully convective stars at accretion rates of $10^{-5} M_{\odot} \text{yr}^{-1}$ and $10^{-4} M_{\odot} \text{yr}^{-1}$, respectively. We also constructed the same initial models following their method and calculated the subsequent evolution at each accretion rate. Figure B1 shows the resulting mass-radius relations. Our calculations agree well with the results presented by Palla & Stahler (1992). For these cases the protostar remains fully convective until just before the swelling, when a radiative barrier appears as for case MD3-D-b0.1 discussed above.

In section 4 we discussed another case with $10^{-4} M_{\odot} \text{yr}^{-1}$ (case MD4-SDm0.1) in addition to that shown in Figure B1. Because the initial models differ, the mass-radius relations are slightly different between these cases, although the adopted accretion rate and boundary condition are the same.

B.2. Comparison with Yorke & Bodenheimer (2008)

Next, we compare the results presented in Section 3.2 to the previous calculations by YB08 (see also discussion in Section 1). YB08 independently calculated the evolution of accreting massive protostars by solving the interior structure using a different numerical code than that used by Palla & Stahler (1992). To make the comparison clear we recalculate the evolution with their code and briefly analyze the evolution of the stellar interior structure. The basic equations are the usual four stellar structure equations, taking into account the effect of mass accretion. The adopted boundary condition slightly differs from the one depicted in equations (2) and (3), but is essentially the same photospheric boundary condition (Bodenheimer et al. 2007; YB08). YB08 solve for a spherical grey stellar atmosphere including curvature effects. The stellar interior models are constructed using the Henyey method iterated to match the grey atmosphere. The initial model is a fully convective $0.1 M_{\odot}$ star of radius $1 R_{\odot}$.

Figure B2 shows the evolution of the stellar radius and interior structure for $\dot{M}_* = 10^{-3} M_{\odot} \text{yr}^{-1}$. The protostar is initially fully convective, until a radiative core appears for $M_* \simeq 0.8 M_{\odot}$. The subsequent evolution is very similar to that for case MD3-D discussed in Section 3.2.1 (see Fig. 4 for comparison). The radiative core gradually grows outward as the stellar mass increases. The D-burning layer, located at the bottom of the outer convective layer, also moves outward. The stellar radius remains $\sim 1 R_{\odot}$ during this phase, which is slightly smaller than for case MD3-D. At this smaller radius (and higher central densities and temperatures) central hydrogen burning occurs earlier than for case MD3-D. The protostar rapidly swells up when $M_* \simeq 4 M_{\odot}$. The radiative core simultaneously expands to cover most of the star. Central hydrogen burning nearly dies out.

As noted in Section 3.2.1, deuterium burning itself is not the cause of the swelling. Figure B2 shows that even if

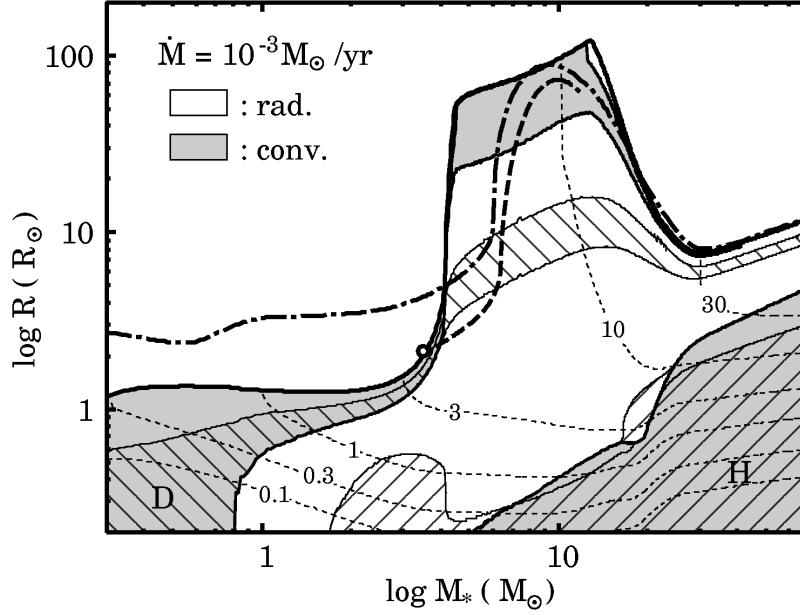


FIG. B2.— Comparison with Yorke & Bodenheimer (2008): The evolution of protostellar radius and interior structure calculated by Yorke & Bodenheimer (2008) for an adopted accretion rate $\dot{M}_* = 10^{-3} M_\odot \text{ yr}^{-1}$. The interior structure is illustrated in the same manner as in the upper panel of Figure 2. The dashed line represents the evolution of the radius after turning off all nuclear reactions when $M_* \simeq 3.5 M_\odot$, indicated on the plot by the open circle. The dot-dashed line shows the evolution of the radius in case MD3-D (taken from Fig. 4).

all nuclear reactions are turned off when $M_* \simeq 3.5 M_\odot$, the protostar significantly swells up later. After the stellar radius reaches its maximum of $120 R_\odot$ when $M_* \simeq 13 M_\odot$, the protostar contracts and hydrogen burning increases in the center. The convective core also grows due to the increased heat input by hydrogen burning. The star reaches the ZAMS for $M_* \simeq 30 M_\odot$ and continues to closely follow the ZAMS as it accretes new material. All these evolutionary features are also seen in case MD3-D. We conclude that the evolution presented in Section 3.2 is fully consistent with the previous calculation by YB08.